An Analysis of Cloud Microphysical Features over UAE Using Multiple Data Sources

Zhenhai Zhang[1], Vesta Afzali Gorooh[1], Duncan Axisa[1], Chandrasekar Radhakrishnan[2], Eun Yeol Kim[2], Venkatachalam Chandrasekar[2], Luca Delle Monache[1]

[1.] *Center for Western Weather and Water Extremes, Scripps Institution of Oceanography, University of California San Diego, La Jolla, CA, USA*

[2.] *Colorado State University, Fort Collins, CO, USA*

Corresponding author: Zhenhai Zhang (zhz422@ucsd.edu)

Abstract. Water is a precious resource and is important for human health, agriculture, industry, and the environment. When water is in short supply, monitoring and predicting the current and future occurrence of precipitating clouds is essential. In this study, we investigate the cloud microphysical features in several convective cloud systems in the United Arab Emirates (UAE) using multiple data sources, including aircraft measurements, satellite observations, weather radar observations, and reanalysis data. The aircraft observation dataset is from an airborne research campaign conducted in August 2019 in the UAE. The cloud cases were identified through analysis of cloud spectrometers mounted on the aircraft. Then, we investigated the microphysical features of those cloud cases with a focus on precipitation microphysics. The effective radius of the cloud particles retrieved from geostationary satellite data was compared with the aircraft in-situ measurement. Using the effective radius retrieved from satellite data, we developed a framework to identify five microphysical zones: diffusional droplet growth zone, droplet coalescence growth zone, supercooled water zone, mixed phase zone, and glaciated zone. The identified zones were verified using the aircraft observations, and the transferability of the 5-zone concept was tested using additional cloud cases. The results show that our 5-zone concept successfully detects the microphysical features related to precipitation using satellite data in the UAE. This study provides scientific support to the development of an applicable framework to examine cloud precipitation processes and detect suitable cloud features that could be tracked for further precipitation analysis and nowcasting.

1. Introduction

Water remains a vital resource globally, with its significance heightened by climate change and an increased frequency of extreme weather events. The availability and sustainability of water resources affect every sector (e.g., Pimentel et al., 2004), particularly in arid or semi-arid regions (Wehbe et al., 2021). In the United Arab Emirates (UAE), the absence of precipitation in the context of growing population over this region in recent years raises concerns about food security and coastline resilience (e.g., Murad et al., 2007). Understanding the physical processes of clouds that trigger precipitation formation is critical for sustainable water management and effective preparation for potential water-related risks.

Most regions in the UAE are arid or semi-arid, and its surrounding areas, except to the north (bordered by the Gulf), are tropical and subtropical deserts (Niranjan Kumar and Ouarda, 2014). The UAE has four climate zones: the Desert Foreland, East Coast, Gravel Plains, and Mountains (Sherif et al., 2014). Most of these zones are characterized by scarce rainfall and a high evaporation rate, except for certain coastal regions. Rainfall distribution within the UAE exhibits large spatial and temporal variation, with the maximum and minimum precipitation occurring in the Mountains and East Coast and the Desert Foreland, respectively (Wehbe et al., 2017). The latter covers the largest portion of the UAE area. The wet season generally occurs from November to April. The average monthly rainfall received by the entire country ranges from approximately 2 mm (e.g., in June) to 15 mm (e.g., in March) (Hussein et al., 2021). The average annual rainfall is generally less than 100 mm, varying from 60 mm to 140 mm (Ouarda et al., 2014; Wehbe et al., 2020). Half of the annual precipitation can fall in a single day during mesoscale convective events (Wehbe et al., 2019; Kumar and Suzuki, 2019).

Due to the extremely low occurrence of rainfall and dry climate, rainfall enhancement is one of the active areas of research in the UAE (Wehbe et al., 2023). While new technologies for weather modification can improve the operational efficiency of rainfall enhancement activities, identifying suitable targets is always a priority (Axisa and DeFelice, 2016, DeFelice and Axisa, 2016, DeFelice et al., 2023, Hirst et al., 2023). Therefore, it is essential to monitor and detect current and future cloud microphysical features related to precipitation processes.

Within convective clouds, precipitation particles are produced by small-scale microphysical processes that are active in different parts of the cloud. These processes initiate

precipitation through multiple physical pathways at different rates. The efficiency by which clouds produce precipitation varies greatly and is a function of the dominant physical process under a specific thermodynamic condition. Growth of precipitation particles can either occur through collision and coalescence or the ice multiplication process or a combination of the two. Raindrops cannot form by diffusional growth alone in convective clouds. The growth of cloud droplets from a radius of 10 to 20 μm to raindrop size (> 100 μm) requires an active collision-coalescence process (Bartlett, 1966). In the absence of collision-coalescence, droplets that form by diffusional growth remain small (i.e., radii < 15 μm) and their size distribution is composed of a high number concentration of small droplets (Pruppacher and Klett, 1998). When these droplets reach temperatures colder than 0°C, they become supercooled and ice can develop through different microphysical pathways. Ice multiplication activity within supercooled clouds is active in the -5° to -8°C region (Hallet and Mossop, 1974) and the rate of production of ice depends not only upon the concentration of large drops (> 24 μm diameter) but also upon the concentration of small drops (< 13 μm) in the cloud (Mossop, 1978). Therefore, the cloud droplet size distribution and parameters derived from it, along with the cloud temperature, are critical to understanding cloud microphysical processes and the dominant physical pathways that lead to precipitation.

Advancement of in-situ and remote sensing technology has provided the cloud physics community with much improved research tools to study aerosol-cloud-precipitation interactions. A combination of satellite cloud top temperature and effective droplet radii, retrieved from the Advanced Very High Resolution Radiometer (AVHRR), has been used to infer the suppression of coalescence and precipitation processes by smoke (Rosenfeld and Lensky, 1998) and desert dust (Rosenfeld et al., 2001). Tropical Rainfall Measuring Mission (TRMM) multi-sensor satellite observations have been used to detect the presence of non-precipitating supercooled liquid water near cloud tops associated with the heavy seeding from smoke over Indonesia (Rosenfeld, 1999) and urban pollution over Australia (Rosenfeld, 2000). The time series of precipitation formation processes within convective storms over the eastern Mediterranean were tracked by METEOSAT Second Generation (MSG) to investigate the cloud response to aerosol loading. A strong correlation was found between the aerosol loading and the depth above cloud base required for the onset of precipitation (Lensky and Shiff, 2007). Aircraft in-situ measurements of continental convective clouds seeded with finely milled salt powder detected a

broadening of the cloud drop size distribution (Rosenfeld et al., 2010), indicating an acceleration of the warm rain process. In addition, aircraft measurements have provided evidence that dust particles extend the tail of the cloud droplet size distribution spectra, increasing the droplet effective radii and triggering the formation of warm rain (Pósfai et al., 2013).

Rosenfeld and Lensky (1998) used the AVHRR satellite data to analyze vertical profiles of the cloud particles' effective radius to investigate the precipitation formation processes in convective clouds and introduced five distinct vertical cloud zones, including (1) diffusional droplet growth zone, (2) droplet coalescence growth zone, (3) rainout zone, (4) mixed-phase zone, and (5) glaciated zone, which characterize the microphysical features of the cloud from the precipitation formation perspective. Lensky and Drori (2007) followed the Rosenfeld and Lensky (1998) approach and defined the temperature of precipitation onset as the temperature where the median effective radius exceeds a threshold of 15 μm. A recent study by Wang et al. (2019) focused on identifying supercooled water clouds and developed a method to detect them based on cloud phase, effective radius, optical thickness, and cloud top temperature from the Advanced Himawari Imager and aircraft in-situ cloud measurements.

During the last two decades, there has been a continuous effort focused on rainfall enhancement science in the UAE (Mazroui and Farrah, 2017; Al Hosari et al., 2021). However, the recent enhanced observations, including the airborne measurements over the UAE (Wehbe et al., 2021; Wehbe et al., 2023) and remote sensing from geostationary satellites (Meteosat-10 and Meteosat-8; Kumar and Suzuki 2019), provide unique data sources to examine the cloud microphysical features and the dominant physical pathways that lead to precipitation in the UAE. Kumar and Suzuki (2019) evaluate the spatial and seasonal occurrence of cloud cover from Meteosat-10 and Meteosat-8 in the UAE, and analyze the cloud phase distribution to determine the potential for precipitation enhancement through cloud seeding with aerosols. In general, cloud seeding is applied using aerosol that is active as a cloud condensation nuclei (CCN) in the warm part of the cloud (called ‘hygroscopic seeding’; Mather et al.,1997; Cooper et al.,1997; Bruintjes, 1999; Terblanche et al., 2000; Silverman, 2000; Silverman, 2003; Rosenfeld et al., 2010; Flossmann et al., 2019), and aerosol that is active as an ice nucleating particle (INP) around supercooled liquid water clouds (called ‘glaciogenic seeding’; Bruintjes, 1999; Silverman, 2001; Woodley et al., 2003a, 2003b; Flossmann et al., 2019). In both hygroscopic and glaciogenic seeding, seeding material must be properly applied to be effective (Geresdi et

al., 2021). This is often referred to as 'targeting'. In practice, this is often the most challenging part of operational seeding programs.

In this study, we investigated the microphysical features of cloud cases over the UAE using multiple data sources focusing on the cloud microphysics of precipitation. We examined these features using aircraft observations, introduced a new 5-zone framework to detect the cloud microphysical zones using satellite data, and used aircraft measurements to validate the detected cloud zones. The corresponding synoptic conditions and the radar reflectivity features for cloud cases were also explored. This study aims to develop an applicable framework that detects cloud features that correspond to microphysical pathways that are active in different parts of the cloud, to characterize precipitation processes in the UAE. One application of this framework is in the development of a tool for further analysis of precipitation and nowcasting, and to assist with cloud targeting in operational seeding programs.

2. Dataset and methodology

2.1 Aircraft observations

The aircraft data is from the UAE 2019 Airborne Campaign (Wehbe et al., 2021; Morrison et al., 2022). The scientific flights in this campaign were conducted by the Stratton Park Engineering Company (SPEC) Learjet 35A in August 2019. This SPEC Learjet 35A aircraft was equipped with state-of-the-art cloud physics instruments. The list of instruments include the following: cloud particle imager (CPI; Lawson et al., 2001); two-dimensional stereo probe (2DS; Lawson et al., 2006); high-volume precipitation spectrometer (HVPS; Lawson et al., 1998); fast forward-scattering spectrometer probe (FFSSP; Brenguier et al., 1998); fast cloud droplet probe (FCDP; Lawson et al., 2017; Woods et al., 2018); and Nevzorov hot-wire probe (Korolev et al., 1998). The FCDP, FFSSP, 2DS, and HVPS were all equipped with probe tips to reduce the effects of ice crystals shattering (Korolev et al., 2011; Lawson, 2011) and data were postprocessed using an interarrival time algorithm to remove shattered particles (Lawson 2011). When combined the cloud particle probes can measure size distributions in the range 2 μm to 2 cm diameter. In this campaign, there were 11 scientific flights (SF) listed in Table 1. Figure 1 shows some examples of the flight tracks, including SF01 on August 12th, SF02 on August 13th, and SF03 on August 18th, 2019. Wehbe et al., (2021) study the evolution of growing convective

cloud tops during this campaign, and present aerosol and cloud microphysical measurements from SF01 and SF04. Morrison et al. (2022) examine microphysical processes with a focus on studying activation and growth of cloud droplets in a bin model, and comparing modeled droplet size distributions with observations for case SF01. In this study we focus on the microphysical properties of SF03 with a focus on the evolution of the drop size distribution and precipitation microphysics.

The aircraft typically targeted growing young turrets in the early stage of the cloud lifetime because they are most valuable to sample for studying the formation of precipitation. Young growing turrets are also most valuable as targets for cloud seeding. Inspection of the forward-looking video from the aircraft confirmed that the clouds sampled are young targets in the early- to mid-life cycle convection. Figure S2 in the Supplement is an example from flight SF03 showing that the aircraft was penetrating a relatively young turret. In addition, we also examined the vertical profiles of radar reflectivity associated with different cloud cases (at the same time and same location as those cases), which suggest that these clouds are relatively young in their lifetime. Figure S1a shows the vertical profiles of radar reflectivity for cloud case SF03. The radar reflectivity ranges from 0 to ~30 dBZ, indicating characteristics of early- to mid-life cycle convection. Our radar observations do not show the high reflectivity (higher than 40 dBZ) typical of mature convection (Zipser et al., 2006; Feng et al., 2018).

During the flight, if the turret was growing, then the turret was profiled vertically through subsequent cloud penetrations in vertical increments in its early- to mid-life cycle stage. Once the cloud top was reached and the cloud transitioned to the past mid-life cycle (or rainout stage), a different and younger cloud target within the same cloud field was selected. This can be distinguished from a change in the altitude of the aircraft within a relatively small radius from the previous location. The forward-looking videos from the aircraft confirm that.

Effective radius (ER) is a weighted average of the size distribution of cloud droplets. In this study we used the combined cloud particle size distribution from FCDP, 2DS, and HVPS to calculate ER following the previous studies (e.g., Rosenfeld et al., 1998; Fu et al., 2022). We use 40 μm as a fixed break point to combine the FCDP and 2DS particle size distribution (Fu et al., 2022). The break point between 2DS and HVPS is 1000 μm. Only size distributions with total number concentrations greater than 10 cm^{-3} are included in calculating ERs (Fu et al., 2022).

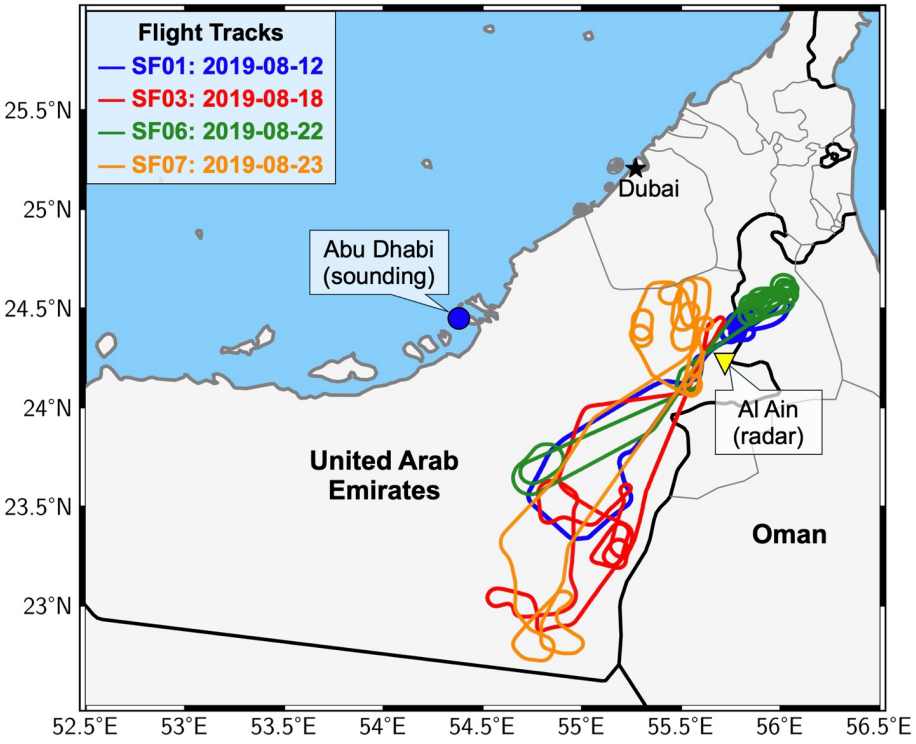

Figure 1. A map showing the flight tracks for SF01 (blue line), SF03 (red line), SF06 (green line), and SF07 (orange line) of the UAE 2019 Airborne Campaign. The yellow triangle is the location of the weather radar in Al Ain and the blue circle is the location of the Abu Dhabi airport where sounding observations are available.

For a better utilization of the aircraft observations, we first identified the measurements of the cloud for each cloud penetration by the aircraft. Figure 2a-b is a time segment of the observed total water content from the Nevzorov hot-wire probe (LWTA) and cloud droplet concentrations from FCDP (ConFCDP) in SF03. When the aircraft penetrated a cloud the LWTA and ConFCDP rapidly increased, as highlighted in the dashed boxes. In this study, if the LWTA is at least 0.05 g m^{-3} and ConFCDP is at least 20 cm^{-3} for one second or longer, it is considered one cloud penetration (CP). Using this definition, we identified the CPs in all 11 flights, and the

numbers of CPs in each flight are listed in the third column of Table 1. Seven of the eleven flights have at least 5 CPs. Several sensitivity tests were conducted to examine the impacts of the thresholds on defining CPs. Different thresholds in the minimum LWTA (0.01 g m^{-3} and 0.1 g m^{-3}) and ConFCDP (10 cm^{-3} and 30 cm^{-3}) did not have any significant impacts on the number of detected CPs since the values of those two parameters in CPs are usually substantially higher than the minimum thresholds (e.g., Figure 2a-b and Figure 5).

After identifying the CPs, we compared selected parameters from different instruments. Figure 2c shows a comparison of liquid water content (LWC) from the FCDP and FFSSP probes with the LWC measured by the Nevzorov probe for the identified CPs in SF03. The Nevzorov probe is a constant-temperature and hot-wire probe designed for measuring the cloud ice and liquid water content, which can provide a relatively more accurate measurement of the water content (Korolev et al., 1998). The LWC from FCDP has a better agreement with the Nevzorov LWC, and their correlation is 0.91, significantly higher than the correlations between the FFSSP and the Nevzorov probes (0.67). Possible reasons for the difference in correlation could be related to sampling bias and/or instrument response, as well as the collection efficiency of droplets in the Nevzorov probe. In this study, we focus on the comparison of the FCDP and FFSSP, both forward scattering spectrometers, with a different instrument that uses other physical properties of droplet sizing, in this case the hotwire mechanism in the Nevzorov LWC. The finding that the FCDP correlates better with the Nevzorov gives us confidence that the FCDP provides higher accuracy compared to the FFSSP.

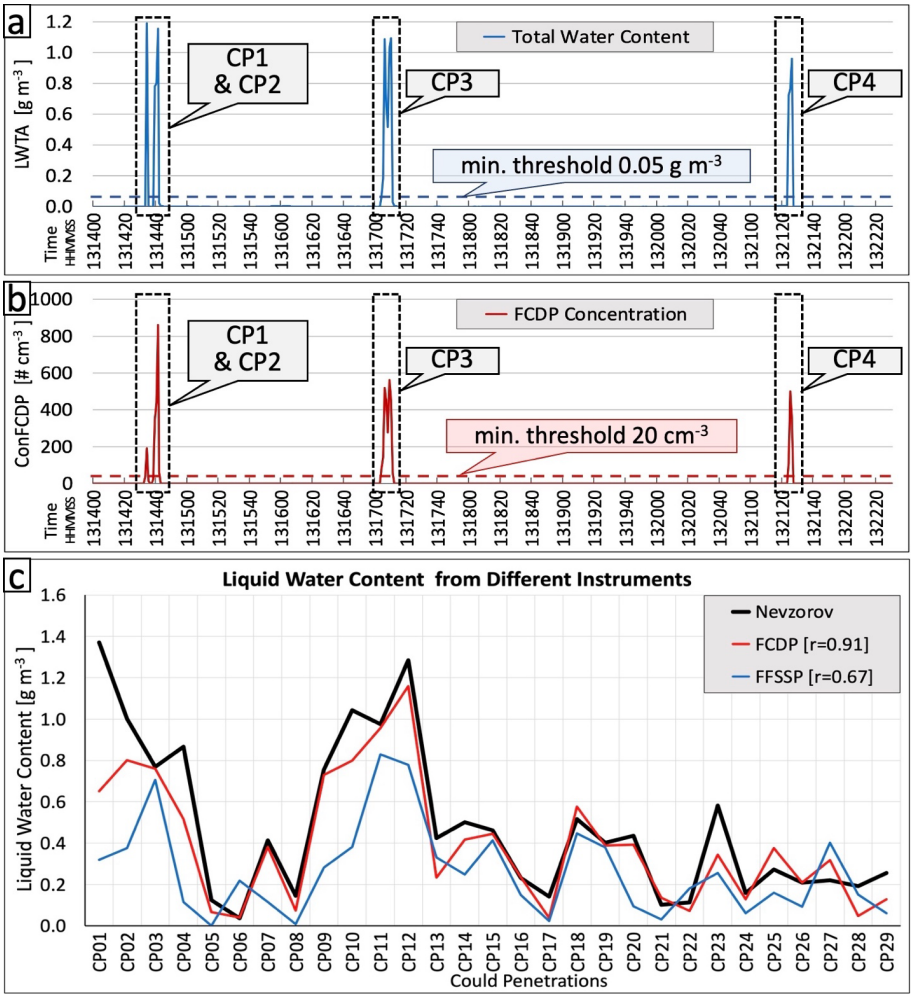

Figure 2. Panels (a) and (b) show examples of cloud penetrations for flight segments when the aircraft penetrated clouds. (a) Time series for total water content (LWTA) and the minimum LWTA threshold (blue dashed line) for cloud penetrations. (b) Time series for cloud particle concentration from FCDP and the minimum FCDP concentration threshold (red dashed line) for cloud penetrations. (c) Comparison of liquid water content from different instruments.

A vertical distribution of the mean effective radius for all the identified CPs in the flights is shown in Figure 3. The mean effective radius here is defined as the average effective radius of all observed values in each cloud penetration. The SF03 has a cloud base at 9.0°C, around 3.5 km of elevation, and the highest/coldest CP is at about -13.0°C, near 6.9 km, indicating a relatively deep cloud. It is worth noting that the cloud top could be higher than the highest CP measured by the aircraft and other colder cloud tops could have been present. The cloud droplet effective radius (ER) is about 4.8 μm at the cloud base and increases with height (decrease of temperature) with a maximum ER of 17.8 μm at -12.9°C. While many cases have a cloud base temperature similar to that of SF03 at around 8.0°C to 9.0°C, SF07 and SF06 have a relatively high measured cloud base with temperatures at 1.8°C and -3.3°C, respectively. All the cloud penetration data for these cases were analyzed, and SF03 was utilized as a prime example to demonstrate our analysis using aircraft observations in Section 3.

UAE 2019 Airborne Campaign				
Flights	**Date**	**Cloud Penetration #**	**Temperature (°C)**	**Mean Effective Radius (μm)**
SF01	2019-08-12	38	-13.6 – 9.3	4.7 – 11.1
SF02	2019-08-13	45	-11.7 – 8.0	3.6 – 17.4
SF03	2019-08-18	29	-13.0 – 9.3	4.4 – 17.8
SF04	2019-08-19	58	-13.1 – 9.3	3.1 – 11.6
SF05	2019-08-20	0	/	/
SF06	2019-08-22	15	-16.1 – -3.2	5.1 – 11.9
SF07	2019-08-23	66	-12.0 – 1.8	3.5 – 10.2
SF08	2019-08-24	5	-9.6 – -8.6	8.3 – 9.3
SF09A	2019-08-26	0	/	/
SF09B	2019-08-26	0	/	/
SF10	2019-08-28	0	/	/

Table 1. A summary of the 11 scientific flights (SFs) in the UAE 2019 Airborne Campaign, including the flight date, number of identified cloud penetrations (CPs), the cloud temperature range of the CPs, and the mean effective radius range of the CPs.

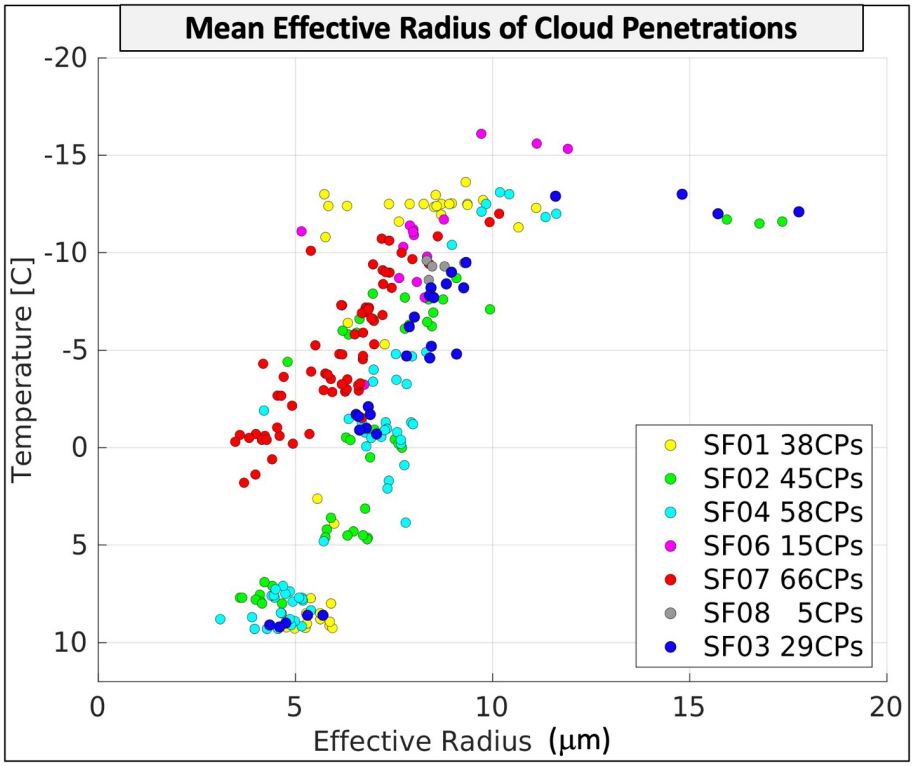

Figure 3. The distribution of the mean effective radius of each cloud penetration. Different colors indicate different scientific flights (SF).

2.2 Satellite products

(a) High Rate SEVIRI Level 1.5 Image Data

Our study uses the near real-time high spatiotemporal resolution data from the Spinning Enhanced Visible and Infrared Imager (SEVIRI) sensor onboard the METEOSAT Second Generation (MSG) satellite (Meteosat-8) with Indian Ocean Data Coverage (IODC). The Visible (VIS), Near Infrared (NIR), and Infrared (IR) bands are geolocated using a standardized projection, resulting in images containing calibrated, radiance linearized, and Earth-located

information, which is appropriate for deriving meteorological products and conducting additional meteorological processing. We use the derived cloud brightness temperature (T) from one IR channel with a center wavelength of 10.8 μm known as a "clean" longwave IR window. This channel is characterized by lower sensitivity to water vapor absorption, enhancing atmospheric moisture correction, and facilitating continuous day/night cloud and convection feature identification. The nominal IR image sampling distance (i.e., spatial resolution) is 3 km by 3 km at the sub-satellite point, and the temporal resolution is 15 mins (96 data points per day).

(b) Optimal Cloud Analysis

This study includes the use of the upper layer cloud effective radius (ER) and cloud phase retrievals from SEVIRI Optimal Cloud Analysis (OCA) algorithm. The OCA method uses reflectance from VIS and NIR channels, radiances from IR channels, the European Centre for Medium-range Weather Forecasts (ECMWF) forecast variables, surface reflectance maps as well as cloud mask products to provide ER ranging from 1 to 31 μm. The SEVIRI OCA scheme is based on an optimal estimation (OE; King et al., 1997; Watts et al., 2011), and it is beneficial for convective cloud monitoring over the Middle East (Mecikalski et al., 2011; Larzi et al., 2014; Hadizadeh et al., 2019). These products rely on the principle that the cloud's optical thickness predominantly determines the reflection function of clouds at a non-absorbing band. In contrast, the reflection function at a water (or ice) absorbing band mainly depends on the size of cloud particles.

Originally formed as a research initiative at the Rutherford Appleton Laboratory (RAL) in 1997, the OCA product has evolved into an operational tool developed by EUMETSAT to deliver timely cloud parameter retrievals from the MSG SEVIRI instrument (Watts et al., 1998). Notably, the OCA product distinguishes itself from alternative retrieval methods by relying on a comprehensive cost function value, indicating consistency between modeling and reality. While some challenges remain, including nighttime performance limitations and constraints in detecting multi-layer conditions for moderate cirrus optical depths, the OCA algorithm is fundamental in advancing our understanding of cloud dynamics and their broader impacts. OCA approaches cloud retrieval as an inverse problem, utilizing a forward model using a radiative transfer model (RTM) to simulate satellite radiances based on a parametrized

cloud/atmosphere/surface model and defined observing conditions. The OE method is then employed to obtain cloud parameters that best match observed radiances, considering measurement errors and prior knowledge (Rodgers, 2000). The OE maximizes the probability of the retrieved state (e.g., cloud effective radius) conditional on the value of the measurements and any a priori knowledge (Poulsen et al., 2012; Watts et al., 2011).

This iterative process aims to minimize a cost function by adjusting the state vector, utilizing the Levenberg-Marquardt scheme for optimization. To initiate the minimization process, the model begins with an initial guess state, typically set to the value of the a priori without additional information. Subsequently, the model iteratively adjusts the state vector in the direction that decreases the cost function at each step, converging toward a minimum. Convergence is reached when the cost function changes minimally between iterations, with unreached convergence deemed as invalid retrievals. The value of the cost function serves as a measure of the solution-state's consistency with observations and prior knowledge, with high or low values indicating potential overestimation or underestimation of error, respectively. It is assumed that measurement errors, a priori parameters, and the forward model follow a Gaussian distribution with a zero mean and covariances.

Phase determination is a crucial aspect of cloud property retrieval, although it is not directly included in the state vector due to its binary nature. In the EUMETSAT OCA approach, the cloud phase is initially assumed to be either ice or liquid based on the calculated overcast brightness temperature of the 11 μm channel, with a threshold of 260 K distinguishing between the two (Mixed phase is not explicitly accounted for in the OCA approach). Throughout the retrieval iteration, the phase may be switched based on specific criteria: a change from liquid to ice occurs when the estimated effective radius exceeds 23 μm, prompting a restart of the retrieval assuming ice phase; conversely, if the effective radius for ice cloud falls below 20 μm, the retrieval is restarted assuming liquid phase.

We acknowledge the uncertainties in satellite ER and phase retrievals. According to the Algorithm Theoretical Basis Document (ATBD) for Optimal Cloud Analysis Product (ATBD for Optimal Cloud Analysis Product, 2016) and supporting algorithm documentation, noise exists in ice ER values due to limitations associated with broken or sub-pixel clouds, as well as mixed-phase or heterogeneous clouds. This noise can result in anomalous ice ER values, such as

unusually large ER values (> 25 μm) or extremely low ER values across all temperatures. In our study, we consider the clouds as ice (hereafter ice cloud), liquid (hereafter water cloud), and total cloud (without any classification). To address the potential misclassification of ice clouds, we implemented a filtering step to exclude any data points where ice retrievals appear at temperatures above 0°C. This adjustment ensures alignment with expected physical characteristics. Additionally, we invite the readers to refer to OCA product guides to contextualize and clarify any observed irregularities in the ER data.

2.3 Other datasets

There are six C-band weather radars covering the UAE region. In this study, the dual-polarization vertical profiles from Al Ain radar (Figure 1) were used to analyze cloud characteristics. The observation area of that radar overlaps with the aircraft observation region. The quality control (QC) procedure was performed before generating the radar's dual-polarization vertical profiles. The QC procedure includes detecting and removing Radio Frequency Interference (RFI), sea clutter, and noise from the data. RFI and sea clutter removal are based on a fuzzy logic algorithm (Liu et al., 2000), and the censoring of noisy data is performed using Signal-to-Noise Ratio (SNR) and Normalized Coherent Power (NCP). After the QC process, the radar data were converted from polar to Cartesian coordinates, with both horizontal and vertical resolutions set at 0.5 km. In the final step, using the location and time of the cloud penetrations conducted by the aircraft we identified coincident observations from the gridded radar data. We applied a 1 km spatial and a 5-minute temporal threshold in the collocation procedure. The radar vertical profiles are generated from the coincident observations.

The latest version of the reanalysis dataset from the European Centre for Medium-Range Weather Forecasts (ERA5; Hersbach et al., 2020) was used in this study to provide an overview of weather conditions for the cloud cases, including the total cloud cover, total column water, and Convective Available Potential Energy (CAPE). The ERA5 data is on a horizontal resolution of about 31 km and 137 vertical levels from the surface up to 0.01 hPa (~80 km). The data used in this study is obtained on 0.25-degree horizontal resolution and hourly temporal resolution. In addition, the temperature sounding profiles observed in the Abu Dhabi airport (Figure 1) are used to identify temperature inversions.

3. SF03 (18 August 2019) case study

3.1 Meteorology

First, a synoptic overview for 18 August 2019 (SF03) was conducted using ERA5 and satellite data (Figure 4) to understand the overall weather conditions, including the total cloud cover, total column water, and Convective Available Potential Energy (CAPE) at 13 UTC from ERA5 and the 3-hour precipitation amount from satellite data at 12-15 UTC. Meanwhile, SF03 was conducted from 12:53 -– 14:31 UTC, and all the CPs were located within the small black box in Figure 4. The atmosphere within this observation area (the small black box) contained a substantial amount of water vapor, measured as 40–45 mm total column water (Figure 4a). The CPs were located on the east side of a strong convection zone (Figure 4b), and the total cloud cover was 40–70% (Figure 4c). Meanwhile, there is a strong temperature inversion layer around 6 km altitude at a temperature of -5°C – -7°C over this area according to the temperature sounding profile observed in the Abu Dhabi airport at 12 UTC and the ERA5 reanalysis (not shown). Temperature inversions are frequently observed during summer in UAE (Weston et al., 2020), which can suppress convection. Based on the precipitation amount derived from satellite data during 12-15 UTC, the SF03 CPs were over the southeast region of a precipitation area (Figure 4d). In this study, we only used the reanalysis to explore the synoptic conditions for the clouds sampled by the aircraft. To identify potential cloud targets for rainfall enhancement applications, high-resolution short-term numerical weather forecasts or nowcasts provide useful information (total column water, CAPE, total cloud cover, etc.) to locate potential areas for convective cloud development.

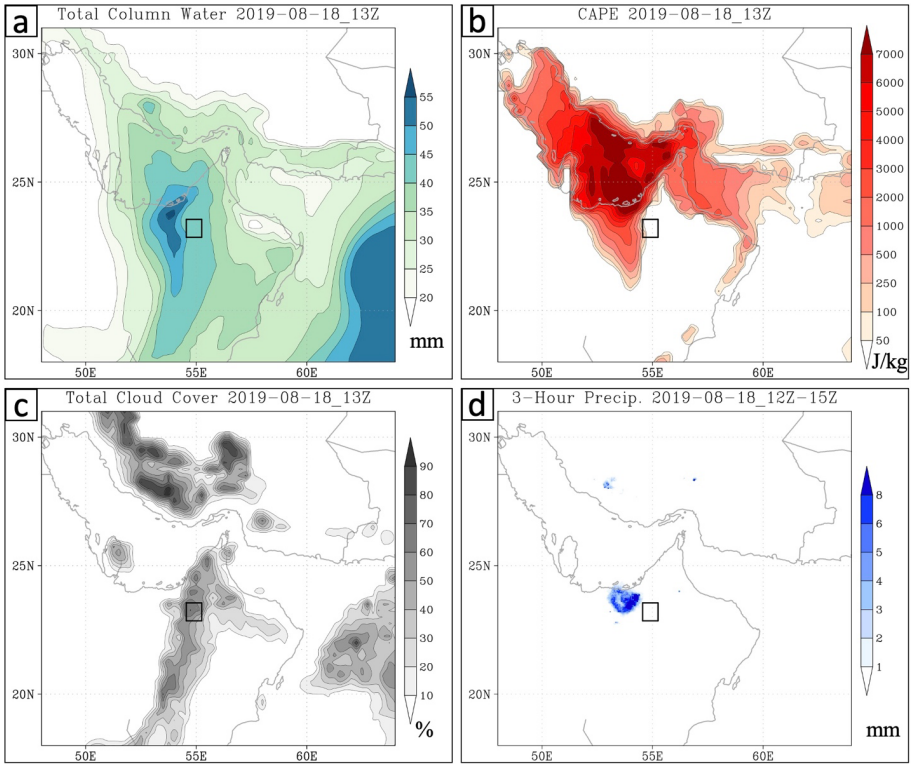

390 Figure 4. (a) the total column water (mm) at 13 UTC on August 18th, 2019, from ERA5 reanalysis; (b) same as (a) but for the Convective Available Potential Energy (CAPE, J/kg); (c) same as (a) but for the total cloud cover (%); (d) the precipitation amount (mm) during 12-15 UTC on August 18th, 2019, from satellite data. The small black box in each panel shows the location of cloud penetrations identified in SF03.

395

3.2 Analysis of cloud microphysical parameters from aircraft observations

Aircraft observations provide detailed measurements of the cloud microphysical properties within clouds. The time series of a few selected parameters from SF03 on August 18th, 2019, was shown in Figure 5 as an example. This flight took off at 12:53 UTC and landed at

400 14:31 UTC. The coincidence of the peak values in total water content from the Nevzorov hot-wire probe and FCDP concentrations showed good agreement in detecting CPs. The first CP

occurred at 13:14:34 UTC with observed peaks in both total water content of 1.19 g m^{-3} and FCDP concentration of 860 cm^{-3} at a temperature of -4.6°C and a height of 5.8 km. The highest (coldest) CP was conducted at 13:26:35 UTC at a height of 6.9 km and a temperature of -13°C with total water content of 0.24 g m^{-3} and FCDP concentration of 48 cm^{-3}. At 14:05:34 UTC, CPs were detected at around 3.6 km height with a temperature of around 9.1°C, and below that, no other CPs were detected, which indicates a cloud base of 3.6 km with a total water content of 0.25 g m^{-3} and FCDP concentration of 1286 cm^{-3}. In total 29 CPs were identified for this case. The mean effective radii (see Figure 3) range from 4.6 to 8.9 μm throughout the vertical profile of the cloud and smaller than the 15 μm threshold for onset of warm rain based on satellite measurements (Lensky and Drori, 2007). Meanwhile, Freud and Rosenfeld (2012) defined 14 μm as the precipitation threshold for warm rain in convective clouds based on aircraft-retrieved data. Although some CPs occurred very close to each other (a few seconds away), all the CPs were identified and processed as independent CP measurements.

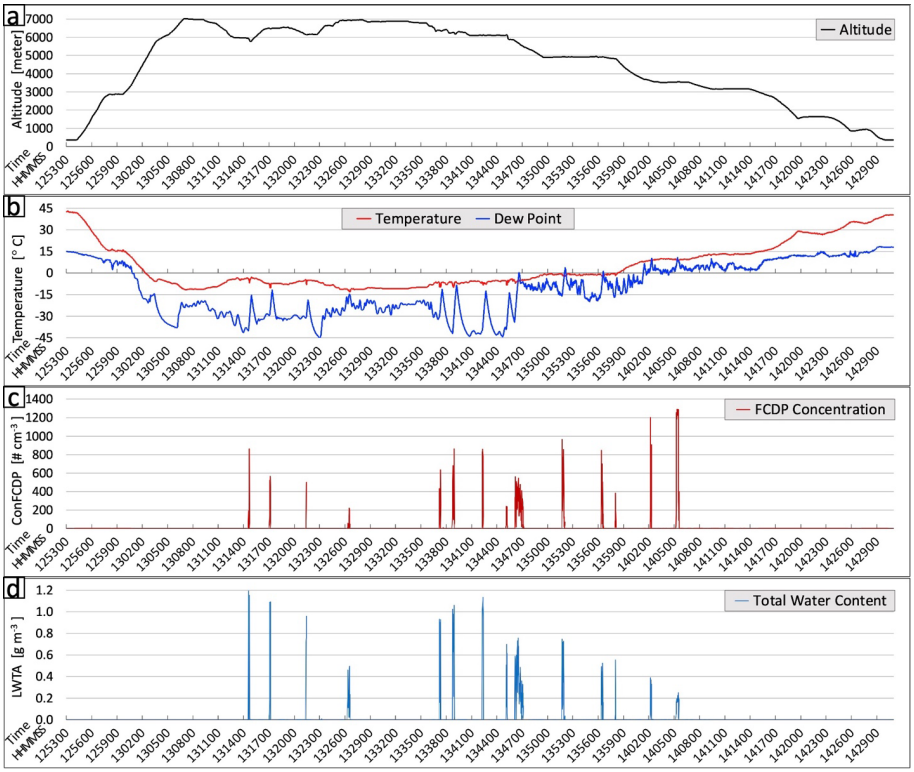

Figure 5. The aircraft observation from SF03, including (a) altitude, (b) temperature and dew point, (c) cloud particle concentration from FCDP, and (d) total water content from Nevzorov probe.

The cloud particle size and the growth rate of the size with height are critical to the formation of rain-sized droplets (Freud and Rosenfeld, 2012). Overall, the ERs of the CPs from SF03 increase with the decrease in temperature (left column of Figure 6). Four CPs from the cloud base to the cloud top are selected for further analysis, including the cloud particle size distributions (middle column), and 2DS and CPI images (right column) from the research aircraft. The first CP (first row of Figure 6) is around the cloud base with a temperature of 9.1°C. Figure 6b shows the corresponding cloud particle size distribution from three instruments: FCDP, 2DS, and HVPS. The FCDP measures the size and number concentration of cloud

droplets in the range of 2 μm to 50 μm diameter (Lawson et al., 2017). This cloud particle size distribution for this CP has the highest concentration at the particle diameter 7–9 μm, decreasing with increasing size (red trace in Figure 6b). The minimum detectable cloud particle size of 2DS is about 10 μm diameter (Lawson et al., 2006; Baker et al., 2009), and number concentrations are in good agreement with the FCDP for cloud particle size larger than 20 μm. Overall, the cloud base penetration with a temperature of 9.1°C has a high droplet concentration at a relatively small size (< 20 μm). This is consistent with the 2DS images for this CP, where large droplets are absent in the 2DS image strips (e.g., Figure 6c). At colder temperatures of -0.7°C (second row of Figure 6), particle size distribution shifts to larger sizes with a maximum concentration of around 10 μm in the FCDP, showing very little droplet growth in the main body of the size distribution in the warm part of the cloud. At a temperature of -5.2°C (third row of Figure 6), the size distribution has a peak concentration at 11 μm, and the 2DS detects a small number concentration (21 per liter) of particles at 50-200 μm in diameter. The 2DS images a few particles around 100 μm in diameter, and the inspection of the CPI shows that these are spherical and around 100 μm in diameter (Figure 6i). At a temperature of -12.1°C (fourth row of Figure 6), there are significantly more cloud particles around or larger than 100 μm based on 2DS with a concentration of 137 per liter (Figure 6k). The 2DS and CPI image particles are ice and larger than 100 μm in diameter (Figure 6l). The observed ice particles indicate an ice production process that is active around -12°C in case SF03.

The noticeable features of these observations are that the cloud base temperature, effective radii, droplet number concentrations, and total water content are typical of high-based continental convective clouds composed of a high number concentration of small droplets formed by diffusional growth of droplets. These droplets have low collision efficiency, and the collision-coalescence process is suppressed as evidenced by the particle size distributions in Figure 6b where the peak concentration and the effective radius is smaller than the 15 μm threshold for warm rain (Lensky and Drori, 2007). The cloud penetration at -12°C indicates that ice production is active at warmer temperatures, which is consistent with ice multiplication within supercooled clouds in the -5° to -8°C region (Hallet and Mossop, 1974) that depends on the ratio of small (diameter < 13μm) to large (diameter > 24 μm) cloud droplets.

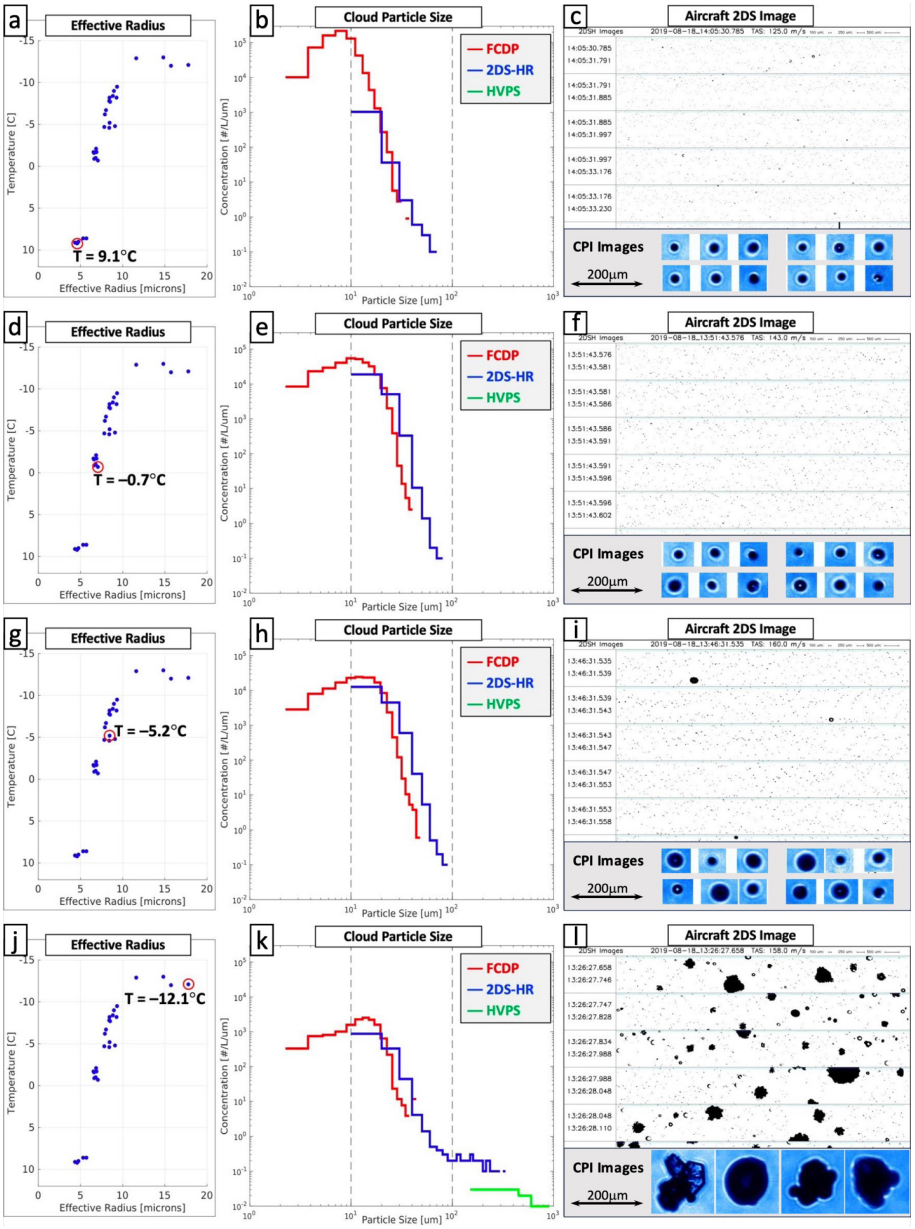
a
Effective Radius
Temperature [C]
Effective Radius [microns]
T = 9.1°C
b
Cloud Particle Size
FCDP
2DS-HR
HVPS
Concentration [#/L/um]
Particle Size [um]
c
Aircraft 2DS Image
CPI Images
200µm
d
Effective Radius
T = −0.7°C
e
Cloud Particle Size
f
Aircraft 2DS Image
CPI Images
200µm
g
Effective Radius
T = −5.2°C
h
Cloud Particle Size
i
Aircraft 2DS Image
CPI Images
200µm
j
Effective Radius
T = −12.1°C
k
Cloud Particle Size
l
Aircraft 2DS Image
CPI Images
200µm

Figure 6. The first row is for the cloud penetration at 9.1°C: (a) the effective radius of each cloud penetration from SF03 and the penetrations at 9.1°C is highlighted in a red circle; (b) the distribution of cloud particle size; (c) 2DS images (top) and CPI images (bottom). (d-f), (g-i), and (j-l) are the same as (a-c) but for cloud penetrations with temperatures of -0.7°C, -5.2°C, and -12.1°C, respectively.

In general, the analysis of cloud microphysical parameters observed in case SF03 agrees with Wehbe et al. (2021) for SF01 and SF04 where the dominance of small-sized particles with diameters less than 10 μm and the minimal concentrations of intermediate sizes (10-30 μm) indicates that an active collision-coalescence process was not achieved. Wehbe et al. (2021) postulated that strong updrafts in SF04 may have carried a limited number of large particles aloft to serve as INP at -10.6°C, but not in SF01. Although the occurrence of first ice cannot be linked to a specific ice nucleation process, ice production is active in SF03. There are many uncertainties associated with the number concentration of ice particles expected within high based continental convective clouds within a certain time, especially in a dusty boundary layer where INP concentrations in the Arabian Basin range up to 2 orders of magnitude at -15°C, between 5×10^{-3} and 5×10^{-1} L^{-1} (Beall et al., 2022). However, the tail in the particle size distribution larger than 100 μm (see Figure 6k) in SF03 is indicative of an active ice production process that is dominant compared to a suppressed collision-coalescence process (see Figure 6b) where the size distribution shows a high number concentration of small droplets.

3.3 Effective radius from satellite data

While aircraft observations can provide detailed measurements to examine the microphysical features of the cloud, it has a limited sample size of measurements and is usually not available for routine assessment of dominant physical pathways that lead to precipitation. Thus, more accessible observation data is needed for real-time applications, such as satellite data. As described in Section 2.2, we retrieved the cloud particle ER for each cloud case using the satellite data from the SEVIRI – METEOSAT 2nd Generation Indian Ocean Dataset.

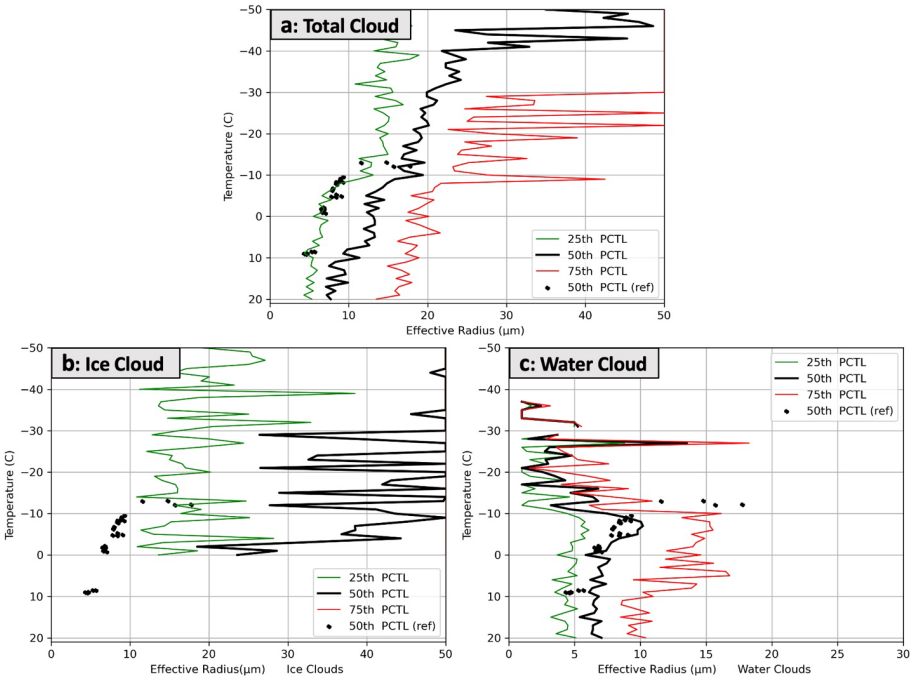

Figure 7. (a) shows the 25th (green line), 50th (black line), and 75th (red line) percentiles of effective radius (ER) for the total cloud in SF03 retrieved from satellite data. (b) and (c) are the same as (a), but for the ice and water clouds from satellite data, respectively. The black dots are the 50th percentile of the ER values in each cloud penetration from aircraft observation.

Before utilizing the ER values retrieved from satellite data, they are validated with the ER measured by aircraft. To ensure the accuracy and relevance of our comparative analysis, the following steps are taken to match the aircraft cloud penetration data with the corresponding satellite data: (1) Temporal Collocation: We applied a temporal threshold of 5 minutes between the aircraft cloud penetrations and the satellite observations to ensure that the measurements were as close in time as possible. This was necessary because of the 15-minute temporal resolution of the products from the SEVIRI sensor onboard the MSG satellite. (2) Spatial Collocation: For spatial collocation, we applied a spatial threshold of 3 km, which allowed us to match the cloud features observed by the aircraft with the satellite data. The aircraft data

provides a high-resolution, detailed view of specific cloud penetrations, and this proximity ensures that the satellite data used for comparison represents the same cloud features. (3) Verification of Collocation: The collocated data points were further verified by comparing the retrieved ERs from both the satellite and aircraft data.

Figure 7 shows the comparison of ERs between the satellite and aircraft datasets for case SF03. In each CP from the research aircraft, the 25^{th}, 50^{th}, and 75^{th} percentile of the ER values are very close to each other because the ER measured from most aircraft CPs are in a short time (one to several seconds/measurements per CP). Therefore, only the 50^{th} percentile of ER values is plotted as black dots in Figure 7. Compared to the satellite-retrieved ERs for total cloud, the aircraft-measured ERs are around the 25^{th} percentile of the satellite ERs (Figure 7a). This is similar to the results from Rosenfeld and Lensky (1998), who showed that the ERs measured by aircraft were mostly around the 25^{th} percentile of the satellite measurements. The ERs measured by aircraft are further compared to the ERs of water clouds and ice clouds from the satellite. The results show that the aircraft ERs are close to the 50^{th} percentile of the satellite ERs for water clouds when the temperature is relatively warm, indicating a fair agreement between these two datasets (Figure 7c). That is because the aircraft derived ERs are highly sensitive to the mode of the size distribution which occurs in the range of the FCDP, which measures the size of particles in the 2-50 μm diameter range and is sensitive to water droplets. It is not surprising that the aircraft ERs tend to be smaller than the satellite ERs for ice clouds due to the lack of sensitivity of the FCDP to ice particles. Overall, the ERs from aircraft and satellite datasets have a fair agreement, which gives us the confidence to use ERs retrieved from satellite data to analyze the relevant cloud features.

This validation is crucial because the ER products are fundamental to understanding cloud microphysical processes, particularly in assessing phase transitions and particle growth mechanisms across different cloud zones. Furthermore, it's important to note that satellite retrievals, especially at certain wavelengths, may introduce artifacts in satellite derived ER values due to phase misclassification, as discussed in the ATBD for OCA Product (ATBD for Optimal Cloud Analysis Product, 2016). To address this, we implemented a filtering step in the satellite data to remove any data points where ice retrievals appear at temperatures above 0°C, ensuring that the ER values remain within physically realistic limits. This adjustment aligns with

findings in Rosenfeld and Lensky (1998), reinforcing the robustness of satellite-derived ER values for microphysical characterization.

3.4 Definition of the Cloud Zones

When there is sufficient data, the next step is characterizing the cloud microphysical features that are indicators of the dominant microphysical processes leading to precipitation. Rosenfeld and Lensky (1998) introduced a 5-zone concept for some cloud cases based on their microphysical features, including diffusional droplet growth zone, droplet coalescence growth zone, rainout zone, mixed phase zone, and glaciated zone. In this study, we follow the Rosenfeld and Lensky (1998) concept and propose a refinement to their methodology. To better represent the early development of convective clouds, we replaced the rainout zone with a supercooled water zone, where supercooled droplets are a hydrometeor type associated with ice production and growth of ice particles to precipitation sizes in mixed-phase convective clouds. In addition, we add the thresholds of brightness temperature, ER, the growth rate of ER, and the cloud phase to define the zones to correspond with basic cloud physics principles described in Section 1.

The accurate classification of these 5-zone relies on physically consistent retrieval of ER values and cloud phases. To enhance reliability, we applied phase-specific thresholds, excluding anomalous ER measurements attributed to phase misclassification (e.g., ice retrievals at temperatures > 0°C), ensuring satellite data represents cloud microphysics. In our analysis, we consider the number of samples for each zone to provide insight into data density, enhancing our understanding of data consistency within each classification. These adjustments are integrated throughout the zones, especially in differentiating water-dominated and ice-dominated regions, and contribute to a clearer distinction between microphysical processes.

Figure 8 is a framework to detect the 5 zones using satellite data. The thresholds in the framework were determined based on the analysis of our case SF03, then tested using different cloud cases (SF01, SF06 and SF07) and validated using aircraft observations (Section 4). The definitions of the 5 zones and the corresponding thresholds for satellite data are listed below.

(1) Zone 1, diffusional droplet growth zone: This zone is usually close to the cloud base with relatively small particle size and very slow growth of particle size. Thus, it is detected using

the satellite data of the water phase cloud and identified when brightness temperature (T) > 0°C and 50th percentile of ER < 10 μm. When this zone exists and is relatively deep, the precipitation-forming processes are suppressed, indicating potential for rainfall enhancement. Our choice of diffusional droplet growth at T > 0°C and RE < 10 μm is based on the cloud ER in the UAE during the summer (2019 August) and aims to identify extreme cases of diffusional growth and to also eliminate cases when coalescence may be marginally active. This is to identify the best targets for cloud seeding using hygroscopic particles, which is most effective in cases when coalescence is not active. When we reference hygroscopic seeding, we assume that the objective is to enhance precipitation. In this case, the hygroscopic particles are ultra giant cloud condensation nuclei (UGCCN), which when introduced at the cloud base and in the updraft region enhance the coalescence of warm-based clouds, accelerating the warm rain process (Rosenfeld et al., 2010).

(2) Zone 2, the droplet coalescence growth zone: The particle size's growth rate in this zone is relatively large, indicating a quick cloud particle growth above the cloud base through a collision-coalescence process. Thus, it is detected using the water phase cloud and identified when T is lower than the coldest temperature in Zone 1 (T_{Z1}) and higher than -10°C, the 75th percentile of ER is between 15 to 20 μm, and the growth rate is relatively large (dER/dT < -0.4 μm per °C). The 75th percentile of ER is used to identify the relatively large droplets developed by collision and coalescence. Although there are still many small droplets, some droplets may start to grow quickly due to coalescence, which will result in a long tail in the droplet size distribution. When Zone 2 exists and is relatively deep, the precipitation-forming processes are active, and the potential for rainfall enhancement using hygroscopic particles (e.g., ultra giant cloud condensation nuclei) is low.

(3) Zone 3, the supercooled water zone: This zone has water particles at a temperature considerably below the freezing temperature, and the growth rate of the particle size is relatively slow. Thus, it is detected using the water phase cloud and identified when 0°C > T > -38°C, the 50th percentile of ER < 20 μm and the growth rate (dER/dT) is between -0.4 – 0.0 μm per °C. The supercooled water zone is designed by the requirements of the cloud seeding operator to conduct hygroscopic and glaciogenic seeding. In glaciogenic seeding, the operators will target supercooled water, even when this supercooled region overlaps with the presence of high coalescence activity. The main difference between Zone 2 and Zone 3 is the

Deleted: microphysical
Deleted: favorable to precipitation initiation
Deleted: microphysical
Deleted: favorable to precipitation initiation

growth rates (dER/dT). When Zone 3 exists and is sufficiently deep, the precipitation-forming processes are usually suppressed, indicating potential for rainfall enhancement by hygroscopic and/or glaciogenic seeding.

(4) Zone 4, the mixed phase zone: This zone has a mixed phase with relatively large particles and rapid particle size growth that usually occurs at relatively low temperatures. Thus, it is detected using satellite data of the total cloud and identified when -10°C > T > -38°C, the 75th percentile of ER > 20 μm, and the growth rate dER/dT < -0.4 μm per °C. Based on the aircraft observation in this UAE campaign in August of 2019, the warmest temperature when ice particles were measured is at least -10°C. Therefore, we use -10°C as the minimum threshold. A deep Zone 4 usually indicates suppressed precipitation-forming processes and potential for rainfall enhancement by glaciogenic seeding.

(5) Zone 5, the glaciated zone: It is a nearly stable zone of ER, and the glaciated particle size is usually large. Thus, it is detected using the ice phase cloud and identified when T is lower than -10°C and the 75th percentile of ER > 25 μm. If Zone 5 exists, the cloud has active precipitation-forming processes, which indicates potential for rainfall enhancement is low.

The 75th percentile of ER is used to identify zones 2, 4, and 5 to detect the relatively large particles in the tail of the particle size distribution that form by coalescence or ice formation. Figure S3 in the Supplement shows an example from one cloud penetration at temperature -5.2°C from SF03. The 75th percentile is more sensitive to those large particles compared to the 50th percentile.

Overall, the 5 zones have different microphysical features, and their definitions are motivated by the requirements of the cloud seeding operator to conduct hygroscopic and/or glaciogenic seeding as labeled in Figure 8. Generally, when the cloud is identified as having suppressed precipitation-forming processes, it could be a suitable target for precipitation enhancement. Conversely when the cloud is identified as having active precipitation-forming processes, it may not be suitable for precipitation enhancement. Figure 8 defines zones by their microphysical features, where precipitation-forming processes active (PFPA) and precipitation-forming processes suppressed (PFPS) are indicated, and the corresponding identification of hygroscopic seeding and glaciogenic seeding patches at the bottom-right corner, which will be discussed in the last section Summary and Discussion.

Deleted: microphysical
Deleted: favorable to precipitation initiation
Deleted: microphysical
Deleted: microphysical
Deleted: microphysical
Deleted: microphysical
Deleted: could be not
Deleted: microphysical
Deleted: M
Deleted: microphysical
Deleted: M

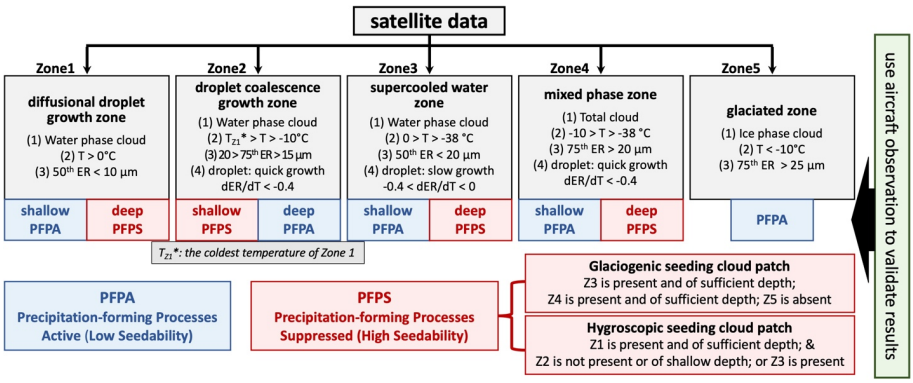

Figure 8. The flowchart of the 5-zone framework, including (1) the diffusional droplet growth zone, (2) the droplet coalescence growth zone, (3) the supercooled water zone, (4) the mixed phase zone, and (5) the glaciated zone. The blue box indicates precipitation-forming processes active (PFPA), and the red box indicates precipitation-forming processes suppressed (PFPS).

An example of a cloud patch at a specific time from SF03 is utilized to demonstrate how to use the 5-zone framework to identify the zones. Figure 9a shows some cloud patches (different colors) from the satellite data on August 18th, 2019, and the one highlighted in a red circle is selected for detecting the zones. Figures 9c-d show the ERs for the water, ice, and total cloud phases. As mentioned before, to provide further context and transparency, we also plotted the number of samples corresponding to each percentile in the figures, which enables a clearer interpretation of the sample size and variability across different cloud types and phases. This inclusion helps highlight the robustness of our satellite-derived ER values, particularly in cases with sufficient data density. In the water cloud, the algorithm detects deep Zone 1 (vertical purple bar) and Zone 3 (vertical cyan bar) layers; and Zone 2 is not detected. In the total cloud, the 75th percentile of ER grows quickly between the temperatures of -37°C and -11°C, identified as Zone 4 (vertical yellow bar). Meanwhile, Zone 5 is identified at a temperature lower than -39°C (vertical orange bar) using the ice clouds satellite data. Overall, due to the present and sufficient depth of Zones 1, 3, and 4, this cloud patch is categorized as precipitation-forming processes suppressed, indicating it is a potential target for rainfall enhancement.

Commented [A1]: Figure updated: using "precipitation-forming processes" instead of "microphysical processes" in the chart and caption.

Deleted: microphysical

Deleted: M

Deleted: microphysical

Deleted: M

Deleted: microphysical

It is worth noting that the satellite data below the cloud base was excluded in Figure 9. The cloud base of this case captured by the aircraft was about 9.1°C (Figure 6a). Meanwhile, according to the Skew-T chart (not shown) from the observed sounding in Abu Dhabi at 00 UTC on the same day of this cloud case (closest sounding observation), the lifted condensation level (LCL, approximating the cloud base) was 15°C. That is warmer than the cloud base temperature captured by aircraft (~9.1°C), possibly due to the differences in time and locations between the sounding and aircraft observations. If the cloud base temperature from a sounding observation at the same time and location as the cloud case is available, it can be used to accurately exclude the satellite data below the cloud base and inhibit the corresponding uncertainties in the depth of the diffusional growth zone (Zone 1) if it is identified.

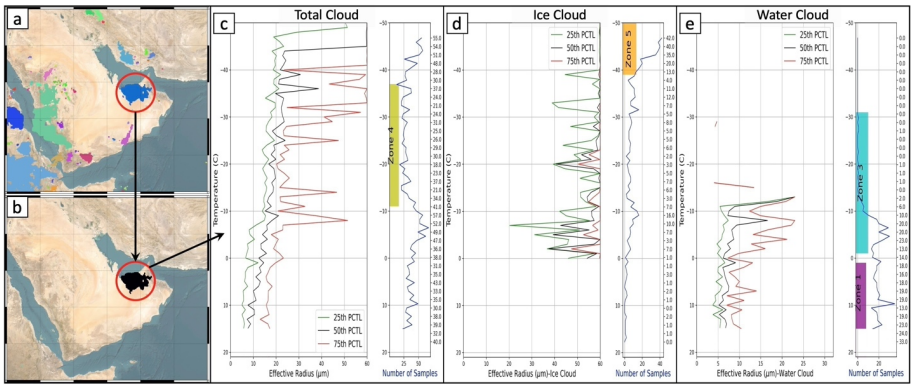

Figure 9. (a) Examples of cloud patches (colors) detected from satellite data. (b) The selected cloud patch for the analysis of effective radius. (c) The effective radius from satellite data for total cloud (left) and the number of data samples (right); the vertical yellow bar represents identified Zone 4, mixed phase zone. (d) is the same as (c) but for the ice cloud and the vertical orange bar represents identified Zone 5, glaciated zone. (e) is the same as (c) but for the water cloud and the vertical purple and cyan bars represent identified Zone 1 (diffusional growth zone) and Zone 3 (supercooled water zone), respectively. The data was excluded if it was below the lifted condensation level (LCL, which approximates the cloud base; 15°C according to the Skew-T observed at Abu Dhabi at 00 UTC on the same day of this cloud case).

Commented [A2]: Figure updated: the data below cloud base (~15C according to the LCL temperature) is excluded,

4. Transferability of cloud zones to other cloud cases

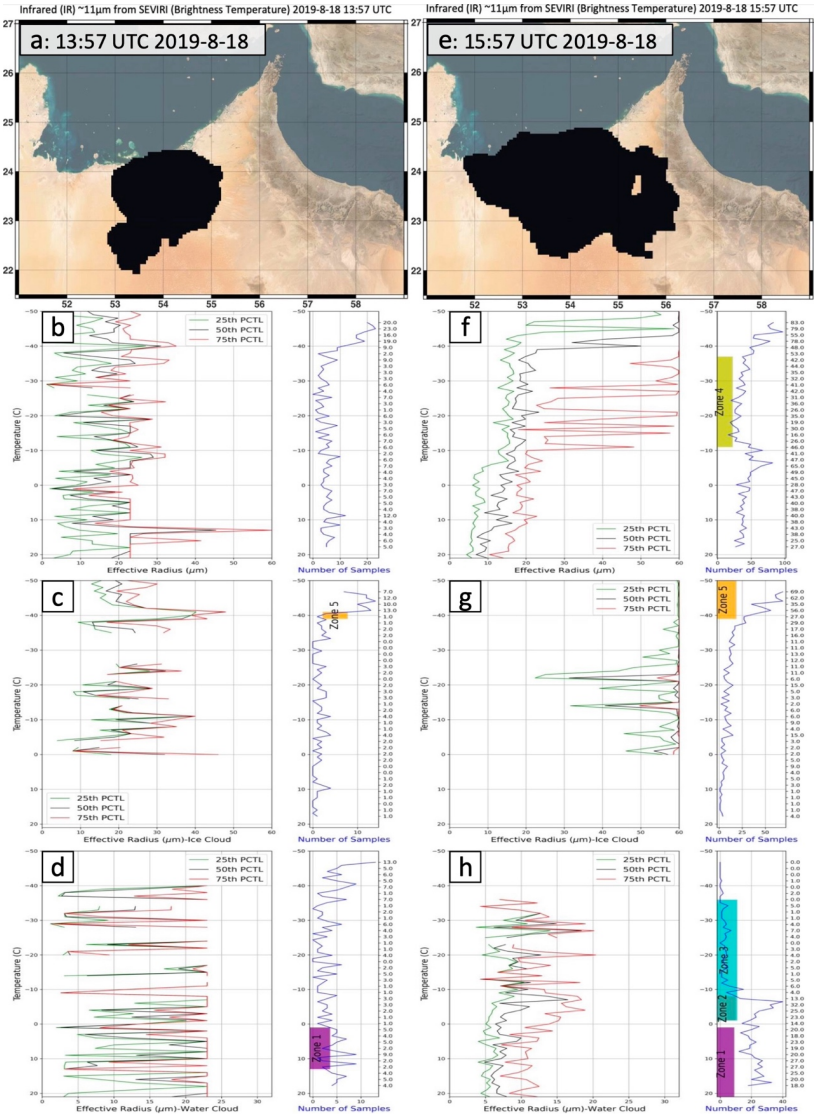

690 Figure 10. The detected zones in one cloud patch on August 18th, 2019. (a) The object of a cloud patch at 13:57 UTC. (b)-(d) The effective radius (left) and the number of data samples (right) for the total, ice, and water cloud phases, respectively. (e)-(h) are the same as (a)-(d) but for the same cloud patch at 15:57 UTC.

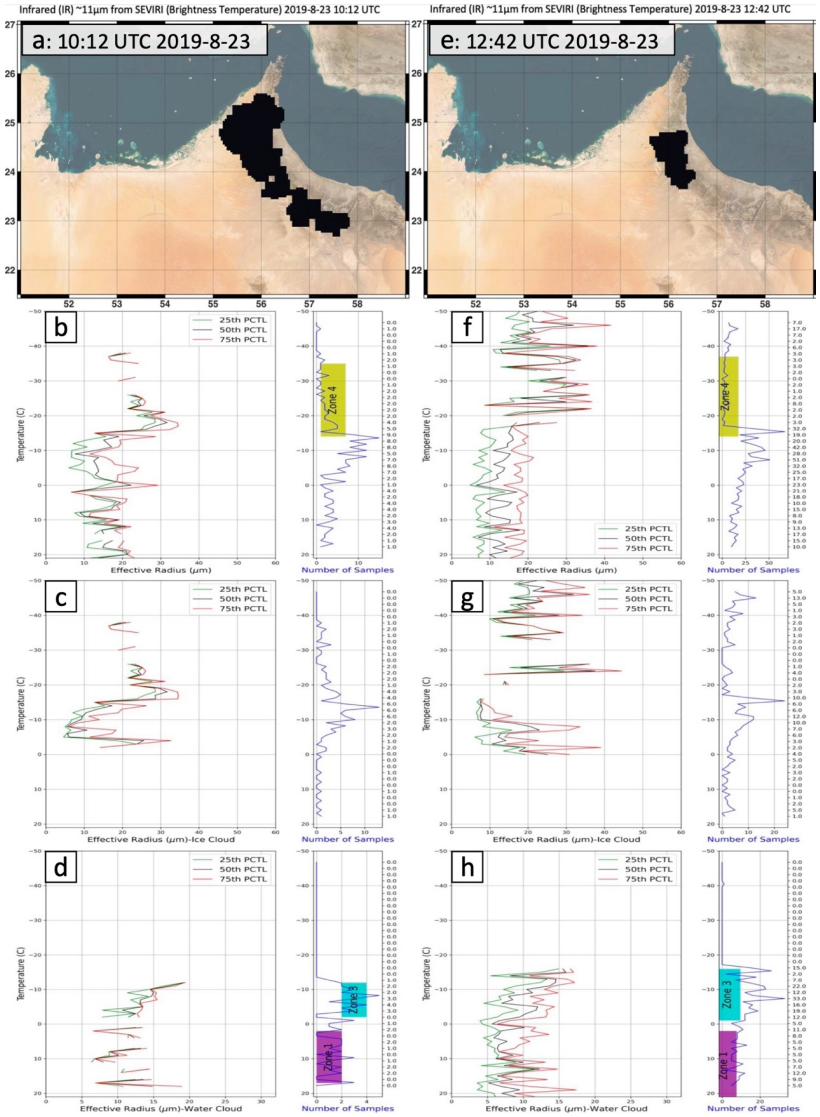

695 Figure 11. Same as Figure 10 but for a cloud patch at (a)-(d) 10:12 UTC and (e)-(h) 12:42 UTC on August 23rd, 2019, (SF07).

In the previous section, we focused on the cloud case of SF03 and introduced the 5-zone framework to identify different cloud microphysical zones. In this section, the 5-zone framework is tested in more cloud cases, and the results are validated using aircraft observation to evaluate the transferability of the 5-zone concept.

First, more examples of the zone detection at specific time points are provided. Figure 10 shows the identification of the zones at two different time points for a developing cloud on August 18th, 2019. In Figure 10a, the black object in the top panel is the cloud patch from satellite data at 13:57 UTC, and Figures 10b-d show the identified Zones 1 and 5 from the satellite data of water and ice clouds, respectively. After 2-hour development, this cloud patch covers a larger area at 15:57 UTC (Figure 10e), and in addition to Zones 1 and 5, Zones 2, 3, and 4 are also detected based on the water and total cloud data (Figures 10f-h). For each cloud zone, we have also included plots of the number of samples, which visually represent sample size across the defined thresholds. In addition to SF03, Figure 11 shows the identification of the zones for the cloud case of SF07 on August 23rd, 2019. At 10:12 UTC, the cloud is mainly over the southwest side of the Al Hajar Mountains, and Zones 1, 3, and 4 are detected in the water and total cloud data (Figures 11a-d). After 2.5 hours, the cloud object becomes significantly smaller, but Zones 1, 3, and 4 still exist at 12:42 UTC (Figures 11e-h).

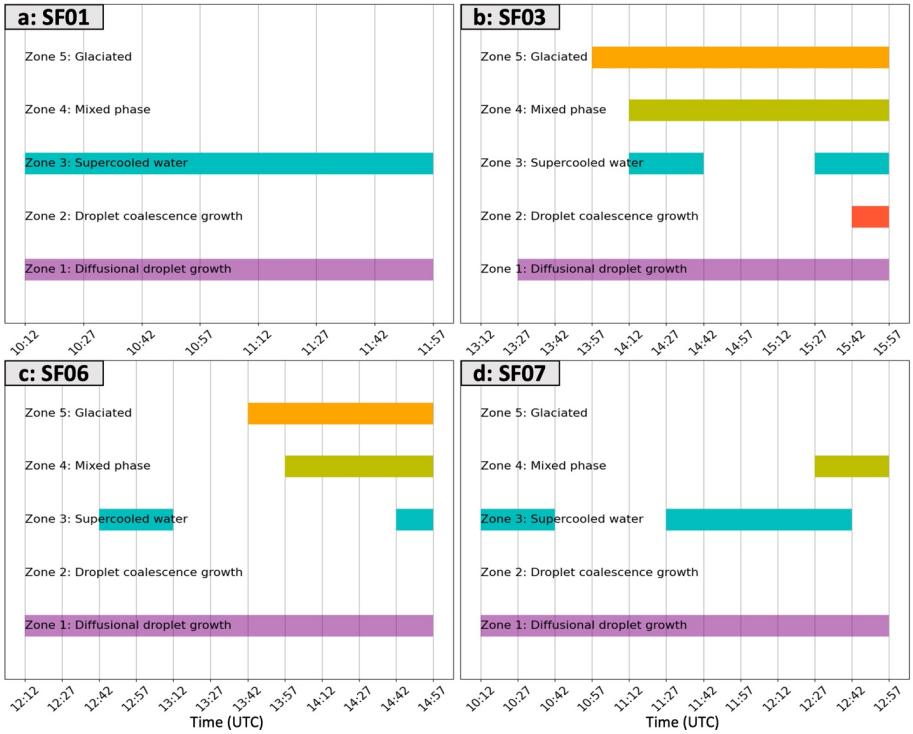

Figure 12. The evolution of the 5 zones in (a) cloud case SF01, (b) cloud case SF03, (c) cloud case SF06, and (d) cloud case SF07. The X-axis is time, and the Y-axis denotes the 5 zones.

The same detection processes can be repeated for any cloud patch through its life cycle to examine the microphysical evolution of the cloud. To test the transferability of the 5-zone concept, the cloud zones are detected using the satellite data through the time periods of the cloud cases SF01, SF03, SF06, and SF07 (Figure 12). These four cases were selected because they have sufficient satellite data to identify the zones and aircraft measurements to validate the results (Figure 13). SF02 and SF04 are not presented here because of limited collocated aircraft data samples and cloudy pixels/points in the satellite images for ice and water phases.

Although all the sampled cloud cases are young targets in the early- to mid-life cycle convection as we previously discussed, there are differences in detected zones across different

cases. In the cloud case SF01 on August 12th, 2019, only Zones 1 and 3 are detected. These zones are detected continuously from 10:12 to 11:57 UTC (Figure 12a), indicating suppressed precipitation-forming processes for this case. The cloud cases SF03 and SF06 have a similar evolution of the zones, including continuous Zone 1, discontinuous Zone 3, and Zones 4 and 5 during the middle and later periods. The difference is that in the case SF03, Zones 4 and 5 develop earlier and last longer, indicating that case SF03 has a more active ice production process. In case SF07, only Zones 1 and 3 are detected for a significant time period, suggesting suppressed precipitation-forming processes.

Deleted: microphysical

Deleted: microphysical

Deleted: for precipitation

To validate the results of the zones based on satellite data, we examined the aircraft observation for those four cloud cases. Case SF03 is intensively examined in Section 3 as an example. Here, to conduct a comparison among the four cases, we selected an aircraft CP with a similar temperature (-12.1°C for the CPs from SF03 and SF07; -12.3°C for SF01; and -12.0°C for SF06) from each case and examined the cloud particle distribution and the 2DS images (Figure 13). A relatively cold temperature (around -12°C) is selected because the main difference among those four cases based on our 5-zone framework is that SF03 and SF06 have Zones 4 and 5, but SF01 and SF07 do not, indicating a difference in the ice production process. The CPs around -12°C are relatively cold for these clouds at the early- to mid-life cycle stage, which presents the best validation for the difference in properties for Zones 4 and 5. The cloud particle sizes from SF01 and SF07 are more concentrated at the relatively small size (Figures 13 a and d). They have a higher concentration (close to or over 10×10^3 per liter per μm) than SF03 (below 3×10^3 per liter per μm) and SF06 (below 8×10^3 per liter per μm) from FCDP in the range 10-20 μm, which implies that the droplet growth in the cloud cases SF01 and SF07 is suppressed. The particle size distribution from 2DS and HVPS in SF03 has a long tail toward the large size, 100 – 1000 μm (Figure 13b), while the distribution in SF06 indicates large particles around 100 μm (Figure 13c). The 2DS image examples in the right column of Figure 13 are in agreement with the cloud particle distribution for particles greater than 20 μm. The 2DS image for SF03 shows many ice particles significantly larger than 100 μm, consistent with the detected continuous Zones 4 and 5 based on satellite data. The 2DS image for SF06 shows a few large particles around or larger than 100 μm, which has fair agreement with the Zones 4 and 5 that exist for a relatively short period. The CPI images for the corresponding CPs for cloud cases SF01, SF03, and SF06 show similar results (right column in Figure 13). The CPI images capture the large ice

particles in SF03 and SF06, while the image for SF01 does not have any large particles. The CPI image for SF07 is not included since it does not have any images available around the time of that CP (within 10 seconds before and after that CP).

Overall, the 5-zone framework identifies the microphysical evolution for all four cloud cases, and the aircraft observations support the identified zones based on satellite data.

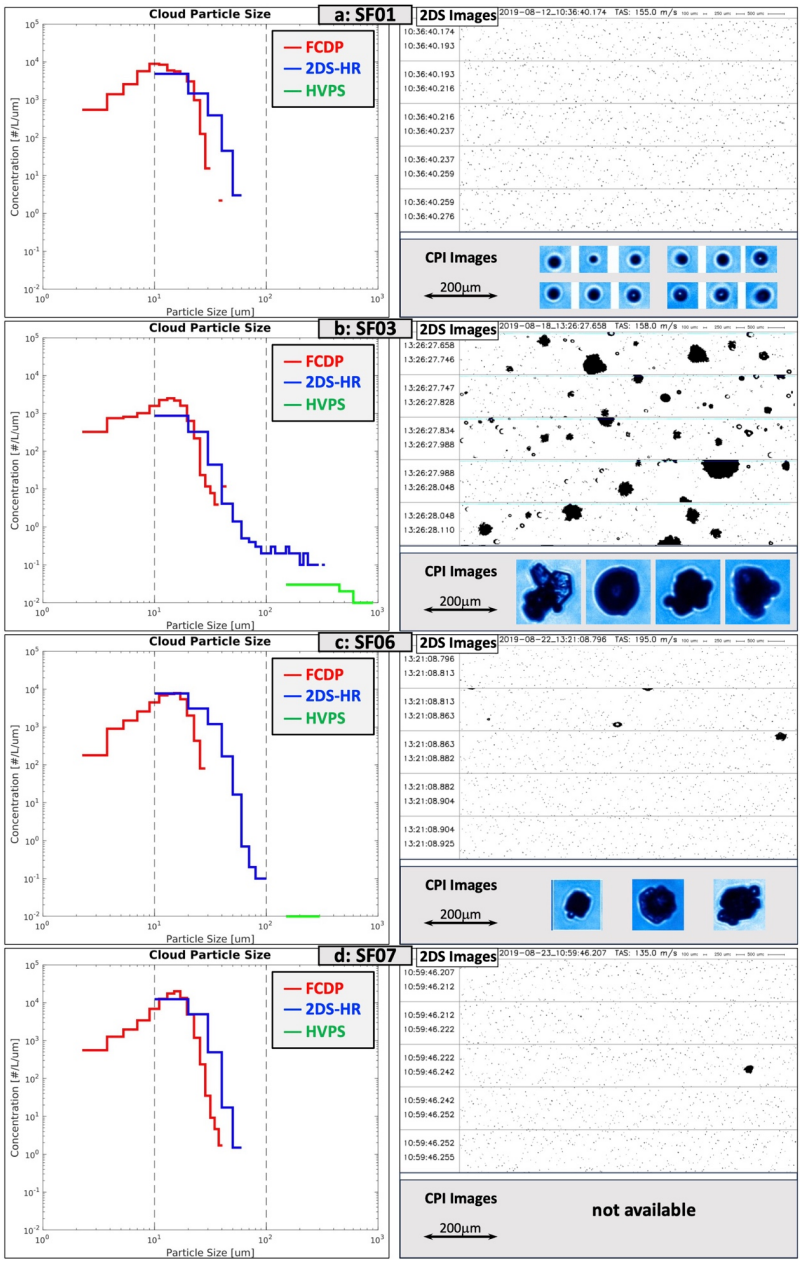
a: SF01
Cloud Particle Size
FCDP
2DS-HR
HVPS
Concentration [#/L/um]
Particle Size [um]
2DS Images
CPI Images
200µm
b: SF03
c: SF06
d: SF07
not available

Figure 13. (a) the distributions of cloud particle size (left) and 2DS images (top right) and CPI images (bottom right) for the cloud penetration at the temperature of -12.3°C in SF01. (b) same as (a) but for the cloud penetration at the temperature of -12.1°C in SF03. (c) same as (a) but for the cloud penetration at the temperature of -12.0°C in SF06. (d) same as (a) but for the cloud penetration at the temperature of -12.1°C in SF07; there are no CPI images.

5. Summary and Discussion

In this study, we investigated the microphysical features for clouds in the UAE using aircraft observations, introduced a 5-zone framework to identify cloud microphysical zones using satellite data, and validated the zones detected from satellite data with aircraft measurements. Our study aims to provide scientific support to develop an applicable framework to examine cloud microphysical processes and detect suitable cloud features that could be targeted for precipitation enhancement in the UAE. A summary of this study is listed below.

1. The UAE 2019 Airborne Campaign provides a unique aircraft sensor dataset, which is analyzed to examine the microphysical features of some cloud cases in the UAE.
2. The effective radius (ER) retrieved from satellite data is in fair agreement with the ER measured by aircraft, adding confidence in using ER data from satellites to analyze the cloud microphysical features.
3. Following Rosenfeld and Lensky (1998), a new 5-zone framework was developed to identify the cloud microphysical zones using satellite data, which can be used to describe the cloud microphysical processes and rainfall enhancement potential.
4. The 5-zone framework can successfully detect the cloud microphysical zones, including the glaciated zone with large ice particles. The results were validated with the aircraft measurements for four cloud cases.

In addition to satellite data, radar data is often used to examine the impacts of cloud seeding (e.g., Vujovic and Protic, 2017; Zaremba et al., 2024; Wang et al., 2021). Meanwhile, the radar data might be a potential data source providing additional information to refine the detection of precipitation-forming processes. We considered radar reflectivity as a supplementary data source to characterize the cloud features related to precipitation. However, only the radar in Al Ain (Figure 1) overlaps with the observation area of three research flights

Deleted: microphysical

(SF03, SF06, and SF07). We explored the potential relationship between the radar reflectivity and the cloud's microphysical features, as summarized in the Supplements. Due to the limited number of available samples, it is difficult to connect the radar data and the cloud microphysical zones. More samples are needed to investigate the potential usage of radar data in detecting the cloud microphysical zones.

The 5-zone framework in this study is based on the 5-zone concept from Rosenfeld and Lensky (1998), but it uses a supercooled water zone instead of the rainout zone since this study focuses on the microphysical processes related to precipitation of convective clouds. In addition, the thresholds of temperature, ER, ER growth rate, and the cloud phase are added for each zone in our framework. We used previous studies (Rosenfeld and Lensky, 1998; Wang et al., 2019) as conceptual references and the data from intensive analysis of cloud case SF03 to determine those thresholds and then refined them through case study analysis of other cloud cases. Since all these cloud cases occur during summer in the UAE, the thresholds determined in this study are considered specific for the summer (primarily convective systems) over the UAE. If this 5-zone framework is utilized for some different seasons or climate zones, a corresponding modification of those thresholds is needed due to the difference in the cloud microphysical features and the environmental aerosols. However, this framework presents a methodology that could be tuned for different seasons and climate zones to identify other cloud types using the threshold parameters identified.

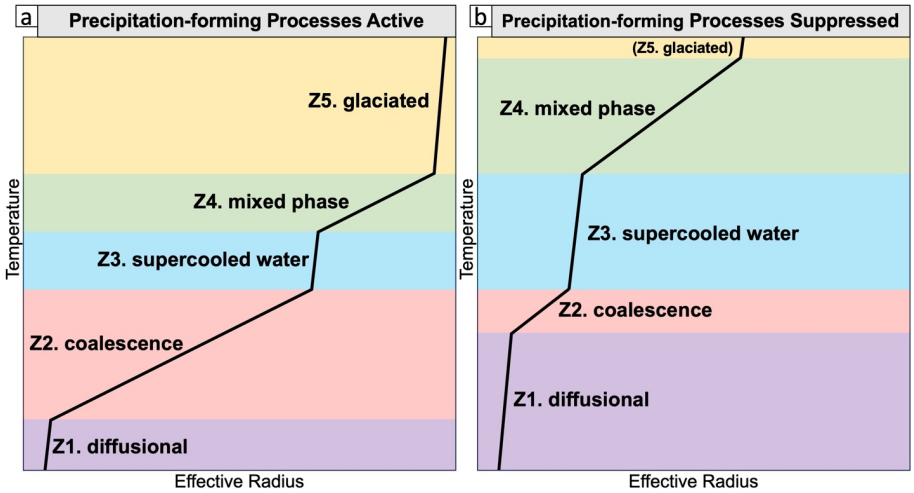

Figure 14. The schematic of the 5 zones for clouds with (a) active precipitation-forming processes and (b) suppressed precipitation-forming processes for precipitation.

The 5-zone framework presents a concept to identify the cloud microphysical zones and diagnose the cloud microphysical processes that affect precipitation. As the concept summarized in Figure 14, this framework focuses on the growth of cloud particle size, which can be quantified using effective radius retrieved from satellite data. While the precipitation-forming processes are active (Figure 14a), such as a deep coalescence zone or the presence of a deep glaciated zone, precipitation may occur efficiently. On the other hand, the precipitation-forming processes are suppressed (Figure 14b), when a deep diffusional growth zone (the coalescence process is suppressed) is present or a deep supercooled water zone (the ice particle production process is not active) is present. In the 5-zone framework, we included thresholds to guide the mode of precipitation enhancement for the cases when suppressed precipitation-forming processes are detected, as shown in red at the bottom of Figure 8. The clouds with suppressed precipitation-forming processes could be a glaciogenic (cold cloud) seeding target if the supercooled water zone is present and has sufficient depth, the mixed phase zone is present and has sufficient depth, or the glaciated zone is absent, which indicates the ice particle production process is not active. On the other hand, the cloud could be a hygroscopic (warm cloud) seeding target if the diffusional droplet growth zone is present and has sufficient depth, the droplet

Commented [A3]: Figure updated: using "precipitation-forming processes" instead of "microphysical processes" in the title and caption.

Deleted: microphysical

Deleted: microphysical

Deleted: microphysical processes favorable to precipitation initiation

Deleted: microphysical processes favorable to precipitation initiation

Deleted: microphysical processes

Deleted: microphysical processes

coalescence growth zone is not present or is shallow, or the supercooled water zone is present, which indicates the cloud droplet collision-coalescence process is suppressed. In addition to determining rainfall enhancement targets for climatological analysis or feasibility studies, this information about seeding mode (hygroscopic and/or glaciogenic) is advantageous in guiding cloud seeding operations in near real time.

In conclusion, this study has successfully introduced and tested a 5-zone framework to identify cloud microphysical zones using satellite data, focusing on cloud microphysical processes related to precipitation and the potential for rainfall enhancement in the UAE during summer. The performance of the framework was demonstrated through the analysis of cloud cases and validated with aircraft measurements. Future work will aim to enhance this approach by incorporating a machine learning-based cloud tracking algorithm applied to MSG data, allowing for a more detailed examination of microphysical zones in near-real time within individually tracked cloud clusters. This advancement will further our understanding of cloud precipitation processes and improve the identification of suitable targets for precipitation enhancement.

Data availability. The ERA5 Reanalysis data can be found on the Climate Data Store website from the Copernicus Climate Change Service, https://cds.climate.copernicus.eu/cdsapp#!/home. The High Rate SEVIRI Level 1.5 Image Data and Optimal Cloud Analysis products are publicly available through EUMETSAT Data Services, https://navigator.eumetsat.int/start.

Competing interests. The authors declare that they have no conflict of interest.

Author contributions. ZZ analyzed cloud microphysical features using aircraft observation data, examined the meteorological conditions using ERA5 data, and wrote the manuscript with contributions from all co-authors. VAG performed the analysis of cloud particle effective radius using satellite data and developed the code to detect the five zones using satellite data. DA conceptualized and supervised this study, and guided the analysis. LDM supervised this study and reviewed the manuscript. CR, EYK, and VC processed the radar data and helped with the interpretation of the radar data.

Acknowledgments. This study is supported by the National Center of Meteorology (NCM), Abu Dhabi, UAE, under the UAE Research Program for Rain Enhancement Science. The authors acknowledge Dr. Paul Lawson and Dr. Brad Baker from the Stratton Park Engineering Company (SPEC) for providing the aircraft observation data from the UAE 2019 Airborne Campaign. The authors also acknowledge Dr. Youssef Wehbe and Dr. Michael Weston from NCM UAE for their review and valuable comments on this manuscript.

References

Al Hosari, T., Al Mandous, A., Wehbe, Y., Shalaby, A., Al Shamsi, N., Al Naqbi, H., ... and Farrah, S.: The UAE cloud seeding program: A statistical and physical evaluation, Atmosphere, 12(8), 1013, https://doi.org/10.3390/atmos12081013, 2021.

ATBD for Optimal Cloud Analysis Product [Online]. Available: https://user.eumetsat.int/s3/eup-strapi-media/pdf_mtg_atbd_oca_b1ba8fc34c.pdf, (accessed: Nov 18 2024), 2016.

Axisa, D., and DeFelice, T. P.: Modern and prospective technologies for weather modification activities: A look at integrating unmanned aircraft systems, Atmos. Res., 178, 114-124, https://doi.org/10.1016/j.atmosres.2016.03.005, 2016.

Baker, B., Mo, Q., Lawson, R. P., O'Connor, D., and Korolev, A.: The effects of precipitation on cloud droplet measurement devices, J. Atmos. Ocean Tech., 26(7), 1404-1409, https://doi.org/10.1175/2009JTECHA1191.1, 2009.

Bartlett, J.T.: The growth of cloud droplets by coalescence, Q.J.R. Meteorol. Soc., 92: 93-104. https://doi.org/10.1002/qj.49709239108, https://doi.org/10.1002/qj.49709239108, 1966.

Beall, C.M., Hill, T.C., DeMott, P.J., Köneman, T., Pikridas, M., Drewnick, F., Harder, H., Pöhlker, C., Lelieveld, J., Weber, B. and Iakovides, M.: Ice-nucleating particles near two major dust source regions, Atmos. Chem. Phys., 22(18), pp.12607-12627, https://doi.org/10.5194/acp-22-12607-2022, 2022.

Brenguier, J. L., Bourrianne, T., Coelho, A. A., Isbert, J., Peytavi, R., Trevarin, D., and Weschler, P.: Improvements of droplet size distribution measurements with the Fast-FSSP (Forward Scattering Spectrometer Probe), J. Atmos. Ocean Tech., 15(5), 1077-1090, https://doi.org/10.1175/1520-0426(1998)015<1077:IODSDM>2.0.CO;2, 1998.

Bruintjes, R.T.: A review of cloud seeding experiments to enhance precipitation and some new prospects, Bull. Am. Meteorol. Soc., 80(5), pp.805-820, https://doi.org/10.1175/1520-0477(1999)080<0805:AROCSE>2.0.CO;2, 1999.

Cooper, W.A., Bruintjes, R.T. and Mather, G.K.: Calculations pertaining to hygroscopic seeding with flares, J. Appl. Meteorol., 36(11), pp.1449-1469, https://doi.org/10.1175/1520-0450(1997)036<1449:CPTHSW>2.0.CO;2, 1997.

Defelice, T. P., and Axisa, D.: Developing the framework for integrating autonomous unmanned aircraft systems into cloud seeding activities, J. Aeronaut. Aerospace Eng., 5(3), 1-6, https://doi.org/10.4172/2168-9792.1000172, 2016.

DeFelice, T. P., Axisa, D., Bird, J. J., Hirst, C. A., Frew, E. W., Burger, R. P., ... and Rhodes, M.: Modern and prospective technologies for weather modification activities: A first demonstration of integrating autonomous uncrewed aircraft systems, Atmos. Res., 106788, https://doi.org/10.1016/j.atmosres.2023.106788, 2023.

Flossmann, A.I., Manton, M., Abshaev, A., Bruintjes, R., Murakami, M., Prabhakaran, T. and Yao, Z.: Review of advances in precipitation enhancement research, Bull. Am. Meteorol. Soc., 100(8), pp.1465-1480, https://doi.org/10.1175/BAMS-D-18-0160.1, 2019.

Freud, E. and Rosenfeld, D.: Linear relation between convective cloud drop number concentration and depth for rain initiation, J. Geophys. Res. Atmos., 117(D2), https://doi.org/10.1029/2011JD016457, 2012.

Geresdi, I., Xue, L., Chen, S., Wehbe, Y., Bruintjes, R., ... and Tessendorf, S. A.: Impact of hygroscopic seeding on the initiation of precipitation formation: results of a hybrid bin microphysics parcel model, Atmos. Chem. Phys., 21(21), 16143-16159, https://doi.org/10.5194/acp-21-16143-2021, 2021.

Hadizadeh, M., Rahnama, M., Kamali, M., Kazemi, M. and Mohammadi, A.: A new method to estimate cloud effective radius using Meteosat Second Generation SEVIRI over Middle East, Adv. Space Res., 64(4), pp.933-943, https://doi.org/10.1016/j.asr.2019.05.035, 2019.

Hallett, J. and Mossop S.: Production of secondary ice particles during the riming process, Nature, 249.5452, 26-28, https://doi.org/10.1038/249026a0, 1974.

Hersbach, H., Bell, B., Berrisford, P., Hirahara, S., Horányi, A., Muñoz-Sabater, J., ... and Thépaut, J. N.: The ERA5 global reanalysis, Q. J. R. Meteorol. Soc., 146(730), 1999-2049, https://doi.org/10.1002/qj.3803, 2020.

Hirst, C. A., Bird, J. J., Burger, R., Havenga, H., Botha, G., Baumgardner, D., DeFelice, T., Axisa, D., and Frew, E. W.: An autonomous uncrewed aircraft system performing targeted atmospheric observation for cloud seeding operations, Field Robotics, 3(1), 687–724, https://doi.org/10.55417/fr.2023022, 2023.

Hussein, K.A., Alsumaiti, T.S., Ghebreyesus, D.T., Sharif, H.O. and Abdalati, W.: High-resolution spatiotemporal trend analysis of precipitation using satellite-based products over the United Arab Emirates, Water, 13(17), p.2376, https://doi.org/10.3390/w13172376, 2021.

King, M.D., Tsay, S.C., Platnick, S.E., Wang, M. and Liou, K.N.: Cloud retrieval algorithms for MODIS: Optical thickness, effective particle radius, and thermodynamic phase, MODIS Algorithm Theoretical Basis Document, 1997.

Korolev, A. V., Strapp, J. W., Isaac, G. A., and Nevzorov, A. N.: The Nevzorov airborne hot-wire LWC–TWC probe: Principle of operation and performance characteristics, J. Atmos. Ocean Tech., 15(6), 1495-1510, https://doi.org/10.1175/1520-0426(1998)015<1495:TNAHWL>2.0.CO;2, 1998.

Korolev, A. V., Emery, E. F., Strapp, J. W., Cober, S. G., Isaac, G. A., Wasey, M., and Marcotte, D.: Small ice particles in tropospheric clouds: Fact or artifact? Airborne Icing Instrumentation

Evaluation Experiment, Bull. Am. Meteorol. Soc., 92(8), 967-973, https://doi.org/10.1175/2010BAMS3141.1, 2011.

Kumar, K.N. and Suzuki, K.: Assessment of seasonal cloud properties in the United Arab Emirates and adjoining regions from geostationary satellite data, Remote Sens. Environ., 228, pp.90-104, https://doi.org/10.1016/j.rse.2019.04.024, 2019.

Lawson, R. P., Stewart, R. E., and Angus, L. J.: Observations and numerical simulations of the origin and development of very large snow- flakes, J. Atmos. Sci., 55, 32092–3229, https://doi.org/10.1175/1520-0469(1998)055<3209:oansot>2.0.co;2, 1998.

Lawson, R. P., Baker, B. A., Schmitt, C. G., and Jensen, T. L.: An overview of microphysical properties of Arctic clouds observed in May and July during FIRE. J, Geophys. Res. Atmos., 106(D14), 14989–15014, https://doi.org/10.1029/2000JD900789, 2001.

Lawson, R. P., and Coauthors: The 2D-S (stereo) probe: Design and preliminary tests of a new airborne, high speed, high-resolution particle imaging probe, J. Atmos. Ocean Tech., 23, 1462–1477, https://doi.org/10.1175/JTECH1927.1, 2006.

Lawson, R. P.: Effects of ice particles shattering on the 2D-S probe, Atmos. Meas. Tech., 4(7), 1361-1381, https://doi.org/10.5194/amt-4-1361-2011, 2011

Lawson, R. P., Gurganus, C., Woods, S., and Bruintjes, R.: Aircraft observations of cumulus microphysics ranging from the tropics to midlatitudes: Implications for a “new” secondary ice process, J. Atmos. Sci., 74, 2899–2920, https://doi.org/10.1175/ JAS-D-17-0033.1, 2017.

Lazri, M., Ameur, S., Brucker, J.M. and Ouallouche, F.: Convective rainfall estimation from MSG/SEVIRI data based on different development phase duration of convective systems (growth phase and decay phase), Atmos. Res., 147, pp.38-50, https://doi.org/10.1016/j.atmosres.2014.04.019, 2014.

Lensky, I. M., and Drori, R.: A satellite-based parameter to monitor the aerosol impact on convective clouds, J. Appl. Meteorol. Climatol., 46(5), 660-666, https://doi.org/10.1175/JAM2487.1, 2007.

Lensky, I. M., and Shiff, S.: Using MSG to monitor the evolution of severe convective storms over East Mediterranean Sea and Israel, and its response to aerosol loading, Adv. Geosci., 12, 95-100, https://doi.org/10.5194/adgeo-12-95-2007, 2007.

Liu, H., and V. Chandrasekar: Classification of Hydrometeors Based on Polarimetric Radar Measurements: Development of Fuzzy Logic and Neuro-Fuzzy Systems, and In Situ Verification, J. Atmos. Ocean Technol., 17, 140–164, https://doi.org/10.1175/1520-0426(2000)017<0140:COHBOP>2.0.CO;2, 2000.

Mather, G. K., Terblanche, D. E., Steffens, F. E., and Fletcher, L.: Results of the South African cloud-seeding experiments using hygroscopic flares, J. Appl. Meteorol., 36(11), 1433-1447, https://doi.org/10.1175/1520-0450(1997)036<1433:ROTSAC>2.0.CO;2, 1997.

Mazroui, A. A., and Farrah, S.: The UAE Seeks Leading Position in Global Rain Enhancement Research, J. Wea. Mod., 49(1), https://doi.org/10.54782/jwm.v49i1.562, 2017.

Mecikalski, J.R., Watts, P.D. and Koenig, M.: Use of Meteosat Second Generation optimal cloud analysis fields for understanding physical attributes of growing cumulus clouds, Atmos. Res., 102(1-2), pp.175-190, https://doi.org/10.1016/j.atmosres.2011.06.023, 2011.

Michael M. Bell, Michael Dixon, Wen-Chau Lee, Brenda Javornik, Jennifer DeHart, Ting-Yu Cha, and Alex DesRosiers.: nsf-lrose/lrose-topaz: lrose-topaz stable final release 20220222 (lrose-topaz-2022022), Zenodo, https://doi.org/10.5281/zenodo.6909479, 2022.

Morrison, H., Lawson, P., and Chandrakar, K. K.: Observed and Bin Model Simulated Evolution of Drop Size Distributions in High-Based Cumulus Congestus Over the United Arab Emirates, J. Geophys. Res. Atmos., 127(3), e2021JD035711, https://doi.org/10.1029/2021JD035711, 2022.

Mossop, S. C.: The influence of drop size distribution on the production of secondary ice particles during graupel growth, Q. J. R. Meteorol. Soc., 104(440), 323-330, https://doi.org/10.1002/qj.49710444007, 1978.

Murad, A.A., Al Nuaimi, H. and Al Hammadi, M.: Comprehensive assessment of water resources in the United Arab Emirates (UAE), Water Resour. Manag., 21, pp.1449-1463, https://doi.org/10.1007/s11269-006-9093-4, 2007.

Niranjan Kumar, K. and Ouarda, T.B.M.J.: Precipitation variability over UAE and global SST teleconnections, J. Geophys. Res. Atmos., 119(17), pp.10-313, https://doi.org/10.1002/2014JD021724, 2014.

Ouarda, T.B., Charron, C., Kumar, K.N., Marpu, P.R., Ghedira, H., Molini, A. and Khayal, I.: Evolution of the rainfall regime in the United Arab Emirates, J. Hydrol., 514, pp.258-270, https://doi.org/10.1016/j.jhydrol.2014.04.032, 2014.

Pimentel, D., Berger, B., Filiberto, D., Newton, M., Wolfe, …, and Nandagopal, S.: Water resources: agricultural and environmental issues, BioScience, 54(10), pp.909-918, https://doi.org/10.1641/0006-3568(2004)054[0909:WRAAEI]2.0.CO;2, 2004.

Poulsen, C. A., Siddans, R., Thomas, G. E., Sayer, A. M., Grainger, R. G., Campmany, E., ... and Watts, P. D.: Cloud retrievals from satellite data using optimal estimation: evaluation and application to ATSR, Atmos. Meas. Tech., 5(8), 1889-1910, https://doi.org/10.5194/amt-5-1889-2012, 2012.

Pósfai, M., Axisa, D., Tompa, É., Freney, E., Bruintjes, R., and Buseck, P. R.: Interactions of mineral dust with pollution and clouds: An individual-particle TEM study of atmospheric aerosol from Saudi Arabia, Atmos. Res., 122, 347-361, https://doi.org/10.1016/j.atmosres.2012.12.001, 2013.

Pruppacher, H.R., Klett, J.D. and Wang, P.K.: Microphysics of clouds and precipitation, https://doi.org/10.1080/02786829808965531, 1998.

Rodgers, C. D.: Inverse methods for atmospheric sounding: theory and practice (Vol. 2), World scientific, 2000.

Rosenfeld, D., and Lensky, I. M.: Satellite-based insights into precipitation formation processes in continental and maritime convective clouds, Bull. Am. Meteorol. Soc., 79(11), 2457-2476, https://doi.org/10.1175/1520-0477(1998)079<2457:SBIIPF>2.0.CO;2, 1998.

Rosenfeld, D.: TRMM observed first direct evidence of smoke from forest fires inhibiting rainfall, Geophys. Res. Lett., 26(20), 3105-3108, https://doi.org/10.1029/1999GL006066, 1999.

Rosenfeld, D.: Suppression of rain and snow by urban and industrial air pollution, Science, 287, 1793–1796, https://doi.org/10.1126/science.287.5459.1793, 2000.

Rosenfeld, D., Rudich, Y., and Lahav, R. Desert dust suppressing precipitation: A possible desertification feedback loop, Proc. Natl. Acad. Sci., 98(11), 5975-5980, https://doi.org/10.1073/pnas.101122798, 2001.

Rosenfield, D., Axisa, D., Woodley, W. L., and Lahav, R.: A quest for effective hygroscopic cloud seeding, J. Appl. Meteorol. Climatol., 49, 1548-1562. doi:10.1175/2010JAMC2307.1, https://doi.org/10.1175/2010JAMC2307.1, 2010.

Sherif, M., Almulla, M., Shetty, A., and Chowdhury, R. K.: Analysis of rainfall, PMP and drought in the United Arab Emirates, Int. J. Climatol., 34(4), 1318-1328, https://doi.org/10.1002/joc.3768, 2014.

Silverman, B.A.: An independent statistical reevaluation of the South African hygroscopic flare seeding experiment, J. Appl. Meteorol., 39(8), pp.1373-1378, https://doi.org/10.1175/1520-0450(2000)039<1373:AISROT>2.0.CO;2, 2000.

Silverman, B.A.: A critical assessment of glaciogenic seeding of convective clouds for rainfall enhancement, Bull. Am. Meteorol. Soc., 82(5), pp.903-924, https://doi.org/10.1175/1520-0477(2001)082<0903:ACAOGS>2.3.CO;2, 2001.

Silverman, B.A.: A critical assessment of hygroscopic seeding of convective clouds for rainfall enhancement, Bull. Am. Meteorol. Soc., 84(9), pp.1219-1230, https://doi.org/10.1175/BAMS-84-9-1219, 2003.

Terblanche, D.E., Steffens, F.E., Fletcher, L., Mittermaier, M.P. and Parsons, R.C.: Toward the operational application of hygroscopic flares for rainfall enhancement in South Africa, J. Appl. Meteorol., 39(11), pp.1811-1821, https://doi.org/10.1175/1520-0450(2001)039<1811:TTOAOH>2.0.CO;2, 2000.

Vujović, D., and Protić, M.: The behavior of the radar parameters of cumulonimbus clouds during cloud seeding with AgI, Atmos. Res., 189, 33-46, https://doi.org/10.1016/j.atmosres.2017.01.014, 2017.

Wang, Z., Letu, H., Shang, H., Zhao, C., Li, J., and Ma, R.: A supercooled water cloud detection algorithm using Himawari-8 satellite measurements, J. Geophys. Res. Atmos., 124(5), 2724-2738, https://doi.org/10.1029/2018JD029784, 2019.

Wang, J., Yue, Z., Rosenfeld, D., Zhang, L., Zhu, Y., Dai, J., ... and Li, J.: The Evolution of an AgI Cloud-Seeding Track in Central China as Seen by a Combination of Radar, Satellite, and Disdrometer Observations, J. Geophys. Res. Atmos., 126(11), e2020JD033914, https://doi.org/10.1029/2020JD033914, 2021.

Watts, P. D., Mutlow, C. T., Baran, A. J., and Zavody, A. M.: Study on cloud properties derived from Meteosat Second Generation Observations, Eumetsat Report, 97, 181, 1998.

Watts, P. D., Bennartz, R., and Fell, F.: Retrieval of two-layer cloud properties from multispectral observations using optimal estimation, J. Geophys. Res. Atmos., 116(D16), https://doi.org/10.1029/2011JD015883, 2011.

Wehbe, Y., Ghebreyesus, D., Temimi, M., Milewski, A., and Al Mandous, A.: Assessment of the consistency among global precipitation products over the United Arab Emirates, J. Hydrol. Reg. Stud., 12, 122-135, https://doi.org/10.1016/j.ejrh.2017.05.002, 2017.

Wehbe, Y., Temimi, M., Weston, M., Chaouch, N., Branch, O., Schwitalla, T., ... and Al Mandous, A.: Analysis of an extreme weather event in a hyper-arid region using WRF-Hydro coupling, station, and satellite data, Nat. Hazards Earth Syst. Sci., 19(6), 1129-1149, https://doi.org/10.5194/nhess-19-1129-2019, 2019.

Wehbe, Y., Temimi, M., and Adler, R. F.: Enhancing precipitation estimates through the fusion of weather radar, satellite retrievals, and surface parameters, Remote Sens., 12, 1342, https://doi.org/10.3390/rs12081342, 2020.

Wehbe, Y., and Temimi, M.: A remote sensing-based assessment of water resources in the Arabian Peninsula, Remote Sens., 13(2), 247, https://doi.org/10.3390/rs13020247, 2021.

Wehbe, Y., Tessendorf, S. A., Weeks, C., Bruintjes, R., Xue, L., Rasmussen, R., ... and Temimi, M.: Analysis of aerosol–cloud interactions and their implications for precipitation formation using aircraft observations over the United Arab Emirates, Atmos. Chem. Phys., 21(16), 12543-12560, https://doi.org/10.5194/acp-21-12543-2021, 2021.

Wehbe, Y., Griffiths, S., Al Mazrouei, A., Al Yazeedi, O., and Al Mandous, A.: Rethinking water security in a warming climate: rainfall enhancement as an innovative augmentation technique, NPJ Clim. Atmos. Sci., 6(1), 171. https://doi.org/10.1038/s41612-023-00503-2, https://doi.org/10.1038/s41612-023-00503-2, 2023.

Weston, M. J., Temimi, M., Nelli, N. R., Fonseca, R. M., Thota, M. S., and Valappil, V. K.: On the analysis of the low-level double temperature inversion over the United Arab Emirates: a case study during April 2019, IEEE Geosci. Remote Sens. Lett., 18(2), 346-350, https://doi.org/10.1109/LGRS.2020.2972597, 2020.

Woods, S., Lawson, R. P., Jensen, E., Bui, T. P., Thornberry, T., Rollins, A., … and Avery, M.: Microphysical properties of tropical tropopause layer cirrus, J. Geophys. Res. Atmos., 123, 6053–6069, https://doi.org/10.1029/2017JD028068, 2018.

Woodley, W.L., Rosenfeld, D. and Silverman, B.A.: Results of on-top glaciogenic cloud seeding in Thailand. Part I: The demonstration experiment, J. Appl. Meteorol. Climatol., 42(7), pp.920-938, https://doi.org/10.1175/1520-0450(2003)042<0920:ROOGCS>2.0.CO;2, 2003.

Woodley, W.L., Rosenfeld, D. and Silverman, B.A.: Results of on-top glaciogenic cloud seeding in Thailand. Part II: Exploratory analyses, J. Appl. Meteorol., 42(7), pp.939-951, https://doi.org/10.1175/1520-0450(2003)042<0939:ROOGCS>2.0.CO;2, 2003.

Zaremba, T. J., Rauber, R. M., Girolamo, L. D., Loveridge, J. R., and McFarquhar, G. M.: On the radar detection of cloud seeding effects in wintertime orographic cloud systems, J. Appl. Meteorol. Climatol., 63(1), 27-45, https://doi.org/10.1175/JAMC-D-22-0154.1, 2024.

Supplement

The Potential Usage of Radar Reflectivity

In addition to the satellite data, the C-band weather radars in the UAE provide another data source to detect cloud features. However, only the radar in Al Ain overlaps with the observation area of three research flights (SF03, SF06, and SF07) and offers continuous vertical profiles of reflectivity. We explored the potential relationship between the radar reflectivity and the cloud's microphysical features. Figure S1a shows the vertical radar reflectivity profiles at the exact location and at the same time with some CPs from SF03, which has the best overlap with the radar data. The reflectivity profiles for the other CPs are not included due to the lack of overlap between the datasets, which might be due to the far distance (around or further than 100 km) from the radar to the locations of those CPs. The reflectivity profiles are categorized into two groups (red and blue) according to their features. The red group captured the reflectivity from ~3.5 km to 13 km, which overlaps (~3.5 – nearly 7.0 km) with the aircraft measurements. In those profiles, the reflectivity value increases with height from ~3.5 km to nearly 7.0 km, related to the increase of cloud particle size with height in the cloud case SF03, as described in Section 3. At the maximum reflectivity near 7 km, the aircraft captured several large ice cloud particles in the 2DS images with 2DS particle concentration reaching 227 per liter at a temperature of -12.9 °C (e.g., Figure S1b). In this cloud case, the maximum reflectivity around 7 km height is a critical layer for ice production. The blue group of reflectivity profiles has little data below 7 km, which means no overlap with the aircraft measurements. Thus, estimating any relationship between those reflectivity profiles and cloud features observed by aircraft is not appropriate.

The radar data could be a valuable source for refining the 5-zone framework. However, the limited number of available samples makes it difficult to build a connection between the radar data and the cloud microphysical zones. More studies are needed to investigate the potential usage of radar data in detecting the cloud microphysical zones.

Figures

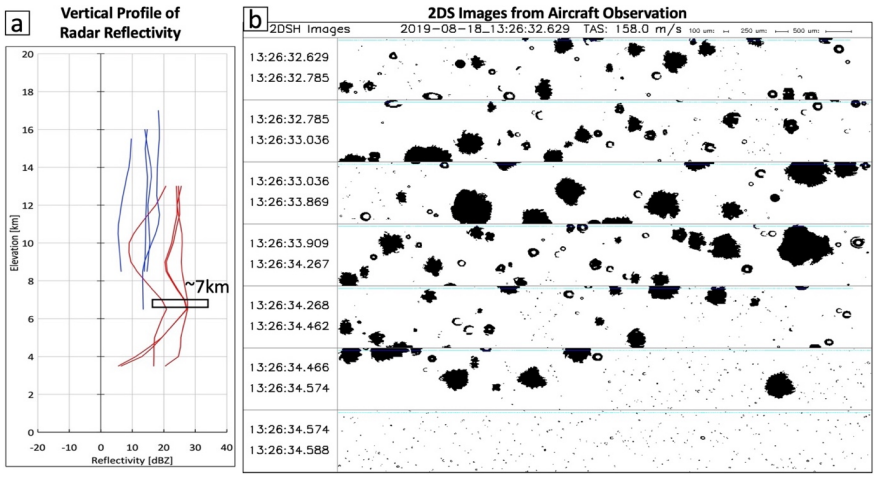

Figure S1. (a) The vertical profiles of radar reflectivity for cloud penetrations in SF03 from the C-band weather radar at Al Ain. (b) The 2-DS image from the aircraft observation at about 7 km elevation.

Figure S2: Image from the aircraft video in flight SF03 on August 18, 2019. The aircraft was penetrating a relatively young cloud turret at 13:41:51 UTC. The temperature measured by the aircraft was -5.7°C at that time.

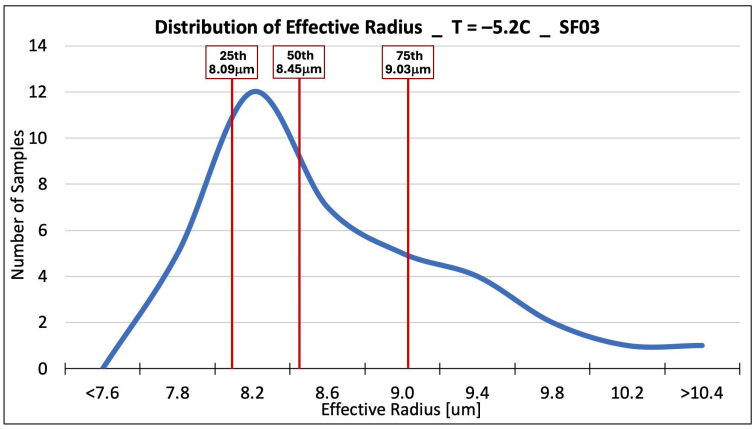

Figure S3: The number of samples distribution of cloud particle effective radius for one cloud penetration at temperature -5.2°C from flight SF03. The three red vertical bars from left to right indicate the 25th, 50th, and 75th percentiles of the effective radius.